

The Structure and Morphology of the Ionized Gas in Starburst Galaxies: NGC5253/5236.¹

Daniela Calzetti

Space Telescope Science Institute, 3700 San Martin Dr., Baltimore, MD 21218, USA; e-mail:
calzetti@stsci.edu

Christopher J. Conselice and John S. Gallagher III

Dept. of Astronomy, University of Wisconsin, 475 N. Charter St., Madison, WI 53706, USA;
e-mail: chris@astro.wisc.edu, jsg@astro.wisc.edu

and

Anne L. Kinney

Space Telescope Science Institute, 3700 San Martin Dr., Baltimore, MD 21218, USA; e-mail:
kinney@stsci.edu

ABSTRACT

We investigate the interplay between starbursts and host galaxies by studying the structure and physical characteristics of the ionized gas surrounding the central starbursts in the two nearby galaxies NGC5253 and NGC5236. The two systems form a pair which presumably interacted about 1 Gyr ago. They represent very different galactic environments, NGC5253 being a metal-poor dwarf, and NGC5236 being a metal-rich, massive, grand-design spiral. We present images of the starburst regions in these two galaxies in the light of the line emission [OIII], H α , and [SII], and in continuum U, V, R.

For NGC5253, the images are deep enough that we can detect faint H α arches and filaments out to ~ 1.9 kpc and [SII] filaments out to ~ 1 kpc from the main ionizing cluster. The ground-based line images are complemented with an archival HST-WFPC2 H β image. Line ratio maps [OIII]/H β and [SII]/H α show that in the outer regions the diffuse ionized gas is partially excited by a non-photoionization process ('shocks'). The 'shocked' gas is mostly concentrated south-west of the galaxy's center, in coincidence with the position of H α bubbles and with extended soft X-ray emission. The H α emission from the shock-excited gas is ≈ 1 –2% of the total and ≈ 10 –20% of the diffuse ionized gas emission, although the mechanical input from the starburst would be sufficient to support a shocked H α luminosity ~ 3 times the observed one. About 80–90% of the diffuse gas is consistent with being photoionized, requiring that about 10% of the ionizing photons escape from the starburst site. The

¹Based on observations obtained at the Las Campanas Observatory of the Carnegie Institution of Washington.

starburst in NGC5253 appears to be fed by gas infalling along the galaxy’s optical minor axis, while hot gas expanding from the starburst has a preferential direction along the major axis.

The results for NGC5236 are less clear than for NGC5253, as the images are not as deep. In the central region of NGC5236, the H α image traces the U emission from the ionizing stars more closely than in NGC5253; the emission line ratio maps show very little or no evidence for presence of shock excitation. Very little or no ionized gas appears expanding from the center of the galaxy outward along the disk plane, and ionization is a local process. The starburst in NGC5236 is thus more strongly confined than that in NGC5253; the deeper gravitational potential well of the more massive galaxy probably keeps the ionized gas near to the ionizing stars.

Subject headings: galaxies: starburst — galaxies: individual (NGC5253, NGC5236) — galaxies: interactions — galaxies: ISM — ISM: structure

1. Introduction

Characterizing the impact of star formation on a galaxy’s ISM is a fundamental step towards understanding the interplay between star formation and gas and, ultimately, the mechanisms responsible for galactic star formation. In a large-scale star formation event, stellar winds and supernova explosions from massive stars generate a feedback mechanism by injecting energy into the ISM, which may produce gas outflows and, in more extreme cases, superwinds (Elmegreen 1992, Silk 1997, Shull 1993, Chu & Kennicutt 1994, Heckman, Armus & Miley 1990). Outflows/superwinds may act as a self-regulating mechanism for the burst, by removing gas from the site of star formation (Heckman 1997, Kennicutt 1989, Meurer et al. 1997). At a less extreme level, OB associations will drive ionization and shock fronts through the ISM, far away from the site of the massive stars, and in some cases causing the star formation process to propagate spatially (Elmegreen & Lada 1977, McCray & Kafatos 1987, Parker et al. 1992, Satyapal et al. 1997, Puxley, Doyon & Ward 1997). Exploring the interactions between a starburst and its surroundings requires studies of components of the host galaxy which are most directly affected by the presence of the starburst. In the optical, the diffuse ionized gas (DIG) is a prime candidate, and in this paper we investigate the ionized ISM in two nearby starburst galaxies, NGC5253 and NGC5236.

The presence of DIG as a general component of the ISM of galaxies is well known (e.g., Monnet, G. 1971). Over the last 15 years, a number of studies have revealed its presence in a large variety of galaxy types: spirals, star-forming irregulars and starbursts (Kennicutt & Hodge 1986, Kennicutt, Edgar, & Hodge 1989, Gallagher & Hunter 1990, Hunter & Gallagher 1992, Hunter & Gallagher 1997, Lehnert & Heckman 1995, Rand 1998, Wang, Heckman, & Lehnert 1998, 1999). Although generally associated with the presence (or past presence) of massive stars, the

DIG can extend over 10 times larger spatial scales than the ionizing stars (Reynolds 1991), and, as a result, the mechanism of ionization of the DIG is still a matter of debate. Photoionization from OB stars appears to account for the Reynold’s Layer (Dove & Shull 1994) and may be a general mechanism for exciting the DIG (Ferguson et al. 1996a, Ferguson, Wyse & Gallagher 1996b, Hunter & Gallagher 1997). This requires that more than 20–30% of the ionizing photons leak out of HII regions. However, the emission line ratios of the DIG are often very different from what is expected from photoionization, and evidence has been accumulating in favor of mixed photoionization/shock, or some other, heating mechanism for the DIG (Sivan, Stasinska, & Lequeux 1986, Hunter & Gallagher 1990, Martin 1997, Rand 1998).

The DIG may be composed of at least two phases: a quiescent one, which comprises 80% of the $H\alpha$ emission and has a scale height comparable to that of stars, and a turbulent one, with a scale height about 3 times that of stars (Wang 1998, Wang, Heckman & Lehnert 1997). These studies demonstrate that the effects of the massive stars extend to galactic scales, and could affect the subsequent evolution of the galaxy. Star formation in starburst galaxies proceeds at a pace that is one-to-two orders of magnitude higher than in “quiescent” galaxies and thus has a major impact on the DIG, as seen in its kinematics, spatial distribution, and ionization (e.g., Marlowe et al. 1995). However, the details are not yet clear as to how the properties of the DIG correlate with the star formation rate of the host galaxy. For instance, does the importance of the DIG increase in a starburst relative to a quiescent galaxy or does it simply become brighter and, therefore, easier to observe (Wang et al. 1998)?

To date, studies of the physical conditions of the ionized ISM in galaxies, and in starbursts in particular, have been pursued mainly via long-slit spectroscopy of a limited number of regions. However, structurally complex objects like starbursts cannot be unraveled without fully accounting for the morphology of both gas and stars. A complementary approach is to use narrow and broad band imaging to obtain a complete map of the gas emission. While the advantage of imaging is to fully characterize the spatial distribution of the ionized gas, the disadvantage is that only the brightest ionized lines can be reasonably imaged with sufficient depth. In addition, the matching of the narrow filter passband with the redshift of the galaxy represents a technical difficulty for large samples of galaxies. Imaging and long-slit spectroscopy provide complementary approaches to the study of the ionized gas in galaxies.

Here we present images of the two nearby starburst galaxies NGC5253 ($v=404$ km/s) and NGC5236 ($v=516$ km/s) in the light of [OIII], $H\alpha$, and [SII]. Variations of the intensity of ionization lines, especially the low ionization ones like [SII], are direct indicators of changing physical conditions of the gas. The two galaxies form a binary pair in the Centaurus group at a distance of a few Mpc (4 Mpc for NGC5253, Sandage et al. 1994). They have completely different characteristics: NGC5253 is a peculiar dwarf (Caldwell & Phillips 1989) and NGC5236 is a massive, grand design spiral, classified as an SABc (Telesco et al. 1993); the two form a metal poor/metal rich pair, with NGC5253 at about $1/6 Z_{\odot}$ and NGC5236 at about $2 Z_{\odot}$. They are both experiencing a high-intensity burst of star formation in their central regions, possibly

triggered by an encounter between the two about 1 Gyr ago. This possibility was first suggested by van den Bergh (1980) on the basis of various evidence, including the warping of the HI disk of NGC5236 (Rogstad, Lockhart & Wright 1974). Thanks to their closeness, these galaxies are excellent laboratories for studying spatial variations of the gas conditions in starbursts; $1''$ corresponds to a linear scale of 19 pc in NGC5253, the size of a typical HII region.

NGC5253 is a “benchmark starburst”, with centrally concentrated recent star formation superimposed on an older, quiescent stellar population. The central star-forming region is very blue, although it is crossed by dust lanes which produce patchy and heavy obscuration and make this galaxy at the same time an excellent UV- and far-IR emitter (Kinney et al. 1993, Aitken et al. 1982, Telesco et al. 1993, Walsh & Roy 1989, Calzetti et al. 1997). Radio observations reveal that a large fraction of the most recent star formation is hidden by dust (Turner, Ho & Beck 1998). The bulk of the ongoing starburst is located in an area 50–60 pc in size, where the stars are about 5 Myr old. The UV emission in this area is dominated by a ~ 3 –4 Myr old stellar cluster, but the ionization is being driven by a ~ 2 Myr old, dust-buried, central cluster (Calzetti et al. 1997, Crowther et al. 1998). The star formation rate (SFR) density of $\sim 10^{-4} M_{\odot} \text{ yr}^{-1} \text{ pc}^{-2}$ corresponds to the maximum levels observed in star-forming galaxies (Meurer et al. 1997). Extending beyond the starburst is a ~ 300 pc region where star formation has been active at a roughly constant level for the last ≈ 100 Myr, with a SFR density about 0.01 of the starburst’s; a handful of bright stellar clusters with ages between 10 and 60 Myr are contained in this area (Calzetti et al. 1997). The ionized gas around the starburst is slowly expanding, with a velocity ~ 10 km/s, at least within the inner 200 pc region (Martin & Kennicutt 1995, see also Strickland & Stevens 1999). The HII emission extends for >1 kpc from the center, with two identified kpc-scale superbubbles in the western periphery, one of them expanding with a velocity of 35 km/s (Marlowe et al. 1995). Moderately high [OIII]/ $H\beta$ ratios in the presence of high [SII]/ $H\alpha$ ratios up to ~ 40 arcsec (800 pc) from the center suggest that shocks or some mechanism other than photoionization contribute to the gas excitation (from long slit spectroscopy, see Martin 1997). The peculiar HI kinematic indicates rotation about the major axis of the galaxy (Kobulnicky & Skillman 1995), but an alternative interpretation, that NGC5253 has accreted/is accreting relatively unprocessed gas along the minor axis, has been suggested to account for the unusually low CO luminosity (Turner, Beck & Hurt 1997).

The starburst in NGC5236 is comparable in intensity to the spectacular event in NGC5253. The central star formation extends for $\sim 20''$ across (~ 360 pc at 3.7 Mpc distance), and is bright at all wavelengths, ranging from X-ray (Trinchieri, Fabbiano & Paulumbo 1985, Ehle et al. 1998), through the UV (Bohlin et al. 1983, Kinney et al. 1993), optical, near-IR (Gallais et al. 1991, Rouan et al. 1996), and mid-IR (Telesco et al. 1993), to the radio (Turner & Ho 1994). The nucleus proper is luminous in the near-IR owing to the large dust obscuration in the center of the galaxy (Gallais et al. 1991, Rouan et al. 1996). Large amounts of dust are present, and form multiple dark lanes which surround the center and cross it in the N-S direction. Gas inflow along the bar collecting at the inner Lindblad resonance may be fueling the central starburst

(Petitpas & Wilson 1998). An optically visible arc of star formation, possibly the main source of the starburst’s UV emission, lies about $6''$ S and SW of the nucleus (Heap et al. 1993, Bohlin et al. 1983). In HST-WFPC1 U-band observations, the arc breaks down into a series of very young star clusters, with ages of $\sim 2\text{--}6$ Myr. The arc-shaped structure could be part of a ring surrounding the nucleus where the other sections are not currently actively forming stars (Gallais et al. 1991). Perhaps star formation has not been co-eval, but sequential, propagating through the ring. Differences between the Br γ EW and CO EW maps support this picture (Puxley et al. 1997). Mid-IR (Telesco et al. 1993) and radio (Turner & Ho 1994) maps depict a different picture. These show two main sources amid diffuse emission: the northern-most source coincides with an optical clump about $11''$ NW of the nucleus and slightly W of the central dust lane, while the southern one is obscured at shorter wavelengths by the dust lane in which it appears to be embedded (Telesco et al. 1993). The detection of only two “point-like” sources at long wavelength led various authors to advocate their extreme youth.

Whatever processes triggered the central starbursts in the two galaxies, they were acting on two very different environments: a grand-design, massive spiral galaxy in NGC5236, and a dwarf in NGC5253. One candidate for the triggering perturbation is the encounter between the two galaxies about 1 Gyr ago (van den Bergh 1980); if this is the case, the timing of the trigger is the same. This would reduce by one the number of free parameters in the problem. The difference between the two environments would then be the major variable, making this pair an important test-bed for starburst studies. This paper therefore focuses on the role of the host galaxy environment on the evolution of the starburst by investigating the physical properties and variations of the large-scale structure of the ionized medium associated with each of the two starbursts. Section 2 describes the observations and data reduction; section 3 presents the analysis of the observations, with special emphasis on nebular line emission; the discussion is contained in section 4 and the conclusions in section 5.

2. Observations and Data Reduction

Broad and narrow band images of NGC5253 (Figure 1) and NGC5236 (Figure 2) were obtained at the 2.5-m telescope of the Las Campanas Observatory with the Direct Camera and a $2k \times 2k$ CCD during the nights of April 28 – May 1, 1997. Broad band images were obtained with 3 in. \times 3 in. filters in the Harris U, V, and R. Narrow band images were obtained using 2 in. \times 2 in. filters on loan from CTIO, centered at the redshifted wavelengths of [OIII] $\lambda\lambda 4959, 5007 \text{ \AA}$, H α + [NII] $\lambda\lambda 6548, 6584 \text{ \AA}$ and [SII] $\lambda\lambda 6717, 6731 \text{ \AA}$ (see Table 1). The platescale on the CCD is $0''.26/\text{pix}$, implying a total field of view of $8'.8$ for the broad band images. The small size of the narrow band filter introduced vignetting at the edges of the CCD, and the final unvignetted field of view was about $5'.2$; the presence of scattered light from the edges of the filters further reduced the useful field of view of the narrow band images to about $4'.7$. The seeing varied during the course of the four nights in the range $0''.9\text{--}1''.2$.

Given the surface brightness variation of more than a factor 100 from the center to the edges of the starburst regions (and more than 10,000 in line emission intensity), the exposure times ranged from 30 s to 600 s in V and R and from 30 s to 1,200 s in U and in the narrow band filters, to achieve suitable exposure levels in different regions of the galaxies. Offsets of a few arcseconds between frames were introduced to remove cosmetic defects (bad pixels and two central bad columns) from the final combined images. Table 2 lists for both galaxies the total exposure time in each filter.

Data reduction followed the standard procedure of bias subtraction, flat-fielding, registration, and co-addition of the images. Both dome and twilight exposures were used to remove pixel-to-pixel variations and illumination patterns from the images. Residual scattered light in the [SII] filter was removed by subtracting a surface fit to the background. The background fit for NGC5253 was adopted for both galaxies, since the background of NGC5236 could not be fit as this galaxy completely fills the field of view. The two central bad columns of the chip were linearly interpolated in each image with values from surrounding columns. Cosmic rays were removed from individual frames before co-addition, using an algorithm developed by M. Dickinson (1997, private communication) for the identification of sharp, positive discontinuities over scales of ~ 1 pix. This technique removed around 80–90% of the cosmic rays; final co-addition of multiple frames removed most of the remaining events. Both galaxies were observed close to their culminating points, and the effects of airmass variations were generally less than 3%; exception were U and [OIII], where such effects were as large as 12% and 5%, respectively, and corrections were therefore applied. Absolute calibrations were obtained from observations of two spectrophotometric standards from Hamuy et al. (1994). One of the standards was also observed during the night at different azimuths to derive airmass corrections. Absolute flux calibrations are listed in Table 1 for all filters, together with the internal error (in percentage).

2.1. Emission Line Images

More than one emission line is included in each of the three narrow band filters. Both the redshifted [OIII] $\lambda 4959$ Å and [OIII] $\lambda 5007$ Å contribute to the emission in the 5000/70 filter; the second line is located almost at the center of the passband, while the [OIII] $\lambda 4959$ Å is located on the ramp, making the determination of its contribution rather uncertain. Our estimates give a best value of $\sim 95\%$ for the filter transmission at the redshifted [OIII] $\lambda 4959$ Å relative to the filter transmission at [OIII] $\lambda 5007$ Å, with a range between 75% and 106%. Three lines, the redshifted H α , [NII] $\lambda 6548$ Å and [NII] $\lambda 6584$ Å, contribute to the emission in the 6563/78 filter, with the reddest [NII] line located at 90% and 72% of the peak transmission for NGC5253 and NGC5236, respectively. Both the redshifted [SII] $\lambda 6717$ Å and [SII] $\lambda 6731$ Å are located close to the transmission peak in the 6737/76 filter.

The calibrated V and R images were used to subtract the stellar continuum from the [OIII], H α + [NII], and [SII] images. After matching the FWHM of the stars in the broad and narrow

band frames, the continuum images were recursively rescaled and subtracted from the narrow band images till optimal removal of the galaxy stellar continuum was achieved. The field stars were initially used to obtain a first guess on the scaling factor, but refinements on this factor were necessary due to the bluer stellar continuum of the galaxies’ centers relative to the stars. For the weak [SII] emission we first subtracted the $H\alpha$ + [NII] nebular emission from the R-band image and then used this nebular emission-free image to remove the stellar continuum from the [SII] image. There is a marked color gradient in the V-band image of NGC5236 with the center bluer than the external regions; therefore accurate continuum subtraction over the entire [OIII] image of NGC5236 could not be achieved. We paid particular attention to the central region, and obtained a satisfactory [OIII] emission line image of the inner $\sim 40''$. This region is comparable in size to the area of $H\alpha$ emission detected above 5σ (see section 3.3 below), and thus is sufficient for our purposes.

The accuracy of the calibration of the narrow band filters was checked against ground-based spectrophotometry of the centers of the galaxies (Storchi-Bergmann, Kinney & Challis 1995) and, for NGC5253, against $H\alpha$ images obtained with the Hubble Space Telescope Wide Field and Planetary Camera 2 (Calzetti et al. 1997). In all cases, our calibrations gave flux values slightly higher than the spectra and the HST image. For NGC5253, our [SII], $H\alpha$ + [NII] and [OIII] fluxes are about 5%, 7% and 10% larger, respectively, than what is measured from the spectrum. For NGC5236, the [SII] and $H\alpha$ + [NII] image fluxes are 8% and 2% larger, respectively, than the spectrum. To compare our $H\alpha$ + [NII] image of NGC5253 with the HST one, the contribution of the [NII] $\lambda 6584 \text{ \AA}$ line had to be removed; from the spectrum we estimate that the [NII] flux is on average 13% of the $H\alpha$ flux, although variations are expected as a function of position (Kobulnicky et al. 1997). After the subtraction of this contribution, our narrow band image gave fluxes consistently $\sim 6\%$ higher than the HST image. The source of this fairly small, but systematic discrepancy is unclear. We have considered under-subtraction of the stellar continuum, filter calibration, and presence of Balmer absorption in the calibration stars, but none of those reproduces all of the observed discrepancy. However, the relative calibration of the three narrow band images is good at the 5% level. For consistency, we rescale our emission line images to the spectroscopic/HST values.

For NGC5253, HST WFPC2 images centered on the $H\beta$ line emission (Calzetti et al. 1997) are used here to supplement the ground based images. The HST $H\beta$ image has been rotated, smoothed, resampled, and registered to match the ground-based images.

3. Analysis and Results

3.1. Line Ratio Maps

Ratios of metal-to-hydrogen lines are common diagnostics of the physical conditions of the ionized gas. We produced maps of [SII] $\lambda\lambda 6717, 6731 \text{ \AA}$ / $H\alpha$ and [OIII] $\lambda 5007 \text{ \AA}$ / $H\beta$ for NGC5253

(Figures 3c, 3e and 3f), and $[\text{SII}]\lambda\lambda 6717, 6731\text{\AA}/\text{H}\alpha$ and $[\text{OIII}]\lambda 5007\text{\AA}/\text{H}\alpha$ for NGC5236 (Figure 4e and 4f). The line ratio maps have been created using a 5σ detection threshold for each line, after all the images have been smoothed to the seeing of the photometrically worst night ($\sim 1''.2$) and resampled to $5\text{ pix}\times 5\text{ pix}$ bins ($1''.3\times 1''.3$). The $[\text{OIII}]\lambda 5007\text{\AA}$ line maps have been divided by a factor 1.3 to remove the contribution from the $[\text{OIII}]\lambda 4959\text{\AA}$. For NGC5236, we don't have an $\text{H}\beta$ emission line image, thus the corresponding ratio map $[\text{OIII}]\lambda 5007/\text{H}\beta$ could not be constructed. We use the $\text{H}\alpha$ image instead, with cautionary remarks about the potentially large effects of reddening variations in the center of the galaxy (see below). We also note that the difficulty of subtracting the continuum from the $[\text{OIII}]\lambda 5007$ image for this galaxy contributes to the larger uncertainty in the line fluxes; a number of the data bins are below our required 5σ threshold, and the 'usable' $[\text{OIII}]\lambda 5007/\text{H}\alpha$ map includes the central $\sim 30''$ region only. This is slightly, but possibly significantly, smaller than the extent of the 5σ $\text{H}\alpha$ ionized region, which occupies the central $\sim 40''$ (see section 3.3). In NGC5253, regions beyond the central $\sim 30''$ in radius have $\text{H}\beta$ flux detections below 5σ , and we have used the $[\text{OIII}]/\text{H}\alpha$ ratio instead, assuming that reddening corrections are small at large distance from the center of the starburst (see discussion below).

3.1.1. Underlying Stellar Absorption

Corrections for the stellar absorption underlying the Balmer lines are important especially at the faintest surface brightness levels, where the EW of the emission line is correspondingly small. We used the ratio of the $\text{H}\alpha$ and the $\text{H}\beta$ emission to the corresponding underlying continua to derive maps of the EW of these lines; for $\text{H}\alpha$ we used the R-band image as continuum, while for $\text{H}\beta$ we used the extrapolated continuum image from the HST V and I images of NGC5253 (Calzetti et al. 1997). The line fluxes were then corrected for the presence of underlying stellar absorption with constant value $\text{EW}=3\text{\AA}$ (e.g., McCall et al. 1985). Figures 3d and 4d show the $\text{H}\alpha$ EW emission maps of the two galaxies, after the correction. Unknown variations of the underlying stellar absorption EW increase the uncertainty in the line flux at the detection threshold, where the emission line EWs are generally small (Figures 3d and 4d). In addition, the contribution of an intermediate/old underlying stellar population proportionally increases as the distance from the center of the starburst (the young population) increases, thus gradually changing the underlying stellar absorption from $\sim 3\text{\AA}$ to $\approx 5\text{\AA}$. The combination of the two effects implies an uncertainty of $\sim 20\%$ and $\sim 50\%$ for the $\text{H}\alpha$ measurements at the detection threshold in NGC5253 and NGC5236, respectively. The variable underlying stellar absorption is taken into account in the following sections every time its effect is relevant to the measurements.

3.1.2. Dust Reddening

Corrections for dust reddening are generally small for the $[\text{SII}]/\text{H}\alpha$ and $[\text{OIII}]/\text{H}\beta$ maps, due to the closeness in wavelength of each pair of lines, but can be large for the $[\text{OIII}]/\text{H}\alpha$, because

the wavelength difference is large. We discuss reddening corrections separately for each of the two galaxies.

Dust extinction in the central $\sim 30'' \times 30''$ of NGC5253 is highly variable (Calzetti et al. 1997); there is a E-W dust lane bisecting the central section of the galaxy and the central ionizing stellar cluster is deeply embedded in a highly opaque dust cloud. We thus use the HST reddening map of Calzetti et al. (1997) to remove extinction effects from the line ratios. We assume the reddening is foreground, which should be a reasonable approximation for most regions, since the $H\alpha/H\beta$ ratio approaches the unreddened case in the vast majority of the bins. However, we already know that the foreground geometry is altogether wrong in the case of the central cluster, where the amount of extinction is above $A_V=10$ mag and the geometry is known not to be foreground (e.g., Beck et al. 1996); such cases should be statistically insignificant when trends between lines are analyzed, as they include a relatively small number of bins. Regions beyond $\sim 30''$ radius, where the HST reddening map is not available, are corrected with the assumption of a small, constant reddening $E(B-V)=0.1$, of which 0.05 are from our Galaxy (Burstein & Heiles 1982). This assumption is reasonable, as the $H\alpha/H\beta$ map indicates that the reddening decreases to small values beyond a radius of $\sim 20''$ from the center (Calzetti et al. 1997).

In the absence of a reddening map for NGC5236, we have adopted the constant value $E(B-V)=0.35$ for the dust extinction correction, which includes both intrinsic and Galactic foreground extinction, as derived from ground-based spectroscopy of the central starburst (Calzetti et al. 1994). Given the small wavelength difference between [SII] and $H\alpha$ the impact of reddening corrections is no larger than 6% for a reddening variation between $E(B-V)=0$ to 0.7. The impact is of course much larger for the $[OIII]\lambda 5007\text{\AA}/H\alpha$; the intrinsic ratio changes by 40% if $E(B-V)=0.7$ instead of 0.35. We know from the study of Telesco et al. (1993) that there is a considerable amount of dust with a complex geometry in the center of NGC5236. For this reason, the $[OIII]/H\alpha$ ratio map, which will be briefly discussed in the next sections, should be considered a preliminary substitute for $[OIII]/H\beta$ for this galaxy.

3.1.3. *The Contribution of [NII] to the $H\alpha$ maps*

The ratio of the HST/ground based $H\alpha+[NII]$ images gives an estimate of the [NII] intensity change across the central region of NGC5253, because the HST image does not contain the $[NII]\lambda 6584\text{\AA}$ emission while the ground based image does. The image ratio appears constant to within 12% in the central $\sim 27''$ (radius), which is where the S/N is high. Thus variations of the [NII] intensity are not expected to be more than twice its average value. This is in agreement with results from long-slit spectroscopy (Lehnert & Heckman 1995, Martin 1997), which indicate that the variation in the $[NII]/H\alpha$ ratio is very small for the central $\sim 25-30''$ of NGC5253 (see, however, Kobulnicky et al. 1997). In the light of this result, we derived a “pure” $H\alpha$ image by removing 17% of the flux from the original image. The 17% figure represents the contribution of the two $[NII]\lambda\lambda 6548, 6584\text{\AA}$ lines.

For NGC5236, the contribution of $[\text{NII}]\lambda\lambda 6548, 6584\text{\AA}$ to the $\text{H}\alpha$ map has been estimated from spectroscopic data (Storchi-Bergmann et al. 1995): the $[\text{NII}]$ line contributes $\sim 39\%$ of the total line flux in the 6563/78 filter, in agreement with the high metallicity of the galaxy.

In the shocked regions of both galaxies, our derived $[\text{SII}]/\text{H}\alpha$ is a lower limit to the true value as $[\text{NII}]/\text{H}\alpha$ is expected to increase for increasing $[\text{SII}]/\text{H}\alpha$, leading to an underestimate of the $[\text{NII}]$ contribution to our $\text{H}\alpha$ maps. This will have in general the effect of weakening the shock diagnostics, an opposite effect to that induced by variable underlying stellar absorption.

3.2. NGC 5253

3.2.1. *The Ionized Gas Morphology*

The morphology of the nebular gas emission in NGC5253 has been described by a number of authors (e.g., Marlowe et al. 1995, Martin & Kennicutt 1995, Calzetti et al. 1997). We review here a few basic facts. The ionized gas emission is circularly symmetric around a stellar cluster located almost at the geometric center of the galaxy (Figure 1, bottom panel); this cluster, with an age of ~ 2 Myr, is also the youngest stellar cluster in the galaxy (Calzetti et al. 1997). The azimuthally-averaged $\text{H}\alpha$ emission monotonically decreases in surface brightness from the cluster outward. The regular morphology of the gas emission is in striking contrast with the morphology of the UV and optical stellar continuum (Figures 3a and 3b), which is elongated from NE to SW, along the major axis of the galaxy (e.g. Martin & Kennicutt 1995). We clearly detect in each of the $\text{H}\alpha$, $[\text{OIII}]$ and $[\text{SII}]$ maps the two western bubbles described in Marlowe et al. (1995): the one closer to the minor axis is the weakest of the two, and we detect the outer shell of the expanding gas; the other, which is almost along the major axis of the galaxy, is well detected and shows a wealth of substructure (Figures 1 and 3). A number of filaments extend outward from the center, both in the North and in the East-South direction. The presence of ionized gas along the dust lane, SE of the center, is detected in both our $\text{H}\alpha$ and $[\text{OIII}]$ images, with a hint in the 5σ $[\text{SII}]$ image.

3.2.2. *Photoionization and Shock-Ionization*

Figure 5 (panel a) shows the line ratios measured in each $1''.3$ resolution element and compares those with models for gas photoionization and for shock excitation. The photoionization models give the variation of the line ratios for changing ionization parameter U . One set of models has been taken from Martin (1997), who ran CLOUDY (Ferland 1993) for a range of metallicities and effective temperatures of the ionizing source. Two other models are from Sokolowski (1993), who analyzed the cases of depleted metal abundances and of hardened photoionizing continuum; the models assume cosmic abundances and an ionizing source given by an instantaneous burst of

star formation with a Salpeter stellar mass function up to $120 M_{\odot}$. The last model reproduces the scenario in which the soft ionizing photons are the first to be absorbed by the ISM, thus the ionizing continuum hardens as it travels across the galaxy. Predicted line ratios for shock excitation are from Shull & McKee (1979), for cosmic abundances and a range of shock velocities and for the special case of depleted metal abundances.

The metal-to-hydrogen line ratios change as a function of the ionization parameter and this can potentially explain the observed variation in Figure 5 (e.g, Hunter 1994). The ionization parameter U measures the relative amount of ionizing photons relative to the amount of gas. Increasing the distance from the ionizing source decreases the value of U , lowering the $[\text{OIII}]/\text{H}\beta$ ratio and increasing the $[\text{SII}]/\text{H}\alpha$ ratio (Domgörgen & Mathis 1994). The data of NGC5253 appear to follow this trend qualitatively both in Figure 5 and in the ionization map $[\text{OIII}]/[\text{SII}]$ of Figure 3g. Except along the dust lane (see discussion below), the $[\text{OIII}]/[\text{SII}]$ ratio decreases from the center to the edges of the ionized region. However, a quantitative comparison (Figure 5, panel a) shows that the $[\text{OIII}]/\text{H}\beta$ value decreases less steeply than expected from variations of the ionization parameter, a trend already noted by Martin (1997) for a sample of dwarf galaxies.

The photoionization model with $T_e=50,000$ K and $[\text{O}/\text{H}]=0.2 [\text{O}/\text{H}]_{\odot}$, which closely matches the metallicity of NGC5253 ($\sim 1/6 [\text{O}/\text{H}]_{\odot}$), marks a lower envelope to the data points in Figure 5, while it is in reasonable agreement with the data at the highest values of U , in regions closest to the central ionizing source in the starburst. A somewhat better representation of the data is given by the model with depleted abundances (Sokolowski 1993), but most of the data points are still above the locus of the photoionization lines. The observed line ratios behave as if there is an increasingly important shock component (Martin 1997) or the radiation spectrum is progressively hardened towards the external regions (Wang 1998).

Ionization in NGC5253 can be directly compared with the well-studied Large Magellanic Cloud. Figure 5, panel (b), shows the $[\text{OIII}]/\text{H}\beta$ versus $[\text{SII}]/\text{H}\alpha$ line ratios of a sample of HII regions, giant and supergiant shells in the LMC from Hunter (1994). Although some of the data points show the same extreme behavior as NGC5253, the majority of the shells agree with photoionization models. The metallicity of the LMC is about twice that of NGC5253, thus the comparison between the two galaxies is not immediate, as the LMC data naturally occupy a locus to the lower left relative to the NGC5253 data. Nevertheless, the majority of the LMC line ratios are between the solar metallicity and the depleted abundances models, and the strongest outliers are in giant shells, which seem to require a hardened radiation field.

To further discriminate between ionization mechanisms, we have plotted the ratios $[\text{SII}]/\text{H}\alpha$ and $[\text{OIII}]/\text{H}\beta$ as a function of the physical distance from the central star cluster in NGC5253 (Figure 6). The mean value of $[\text{SII}]/\text{H}\alpha$ ($[\text{OIII}]/\text{H}\beta$) increases (decreases) for increasing distance from the ‘center of ionization’. Again, photoionization models reproduce qualitatively, but not quantitatively, this trend. The relationship between ionization parameter and distance has been taken from Martin (1997, see her Equation 1); the size of the ionized sphere has been assumed

to correspond to the size of the $H\alpha$ emission, around $71''$ – $81''$ in radius, or 1.4–1.6 kpc. A quantitative test shows that photoionization alone cannot fully explain the observed trend of the line ratios, and, in particular, cannot account for the increasing *spread* about the mean values with increasing distance. The increasing spread with distance is quite evident in the $[OIII]/H\beta$ diagram (Figure 6b). We interpret this as an effect of the increasing importance of shock-ionization (or other non-photoionization mechanism, see Haffner, Reynolds & Tufté 1999) over photoionization further from the center. The physical extent of the starburst and metallicity variations may play a role in the line ratio spread, but we do not expect these to be the dominant effects. We will show in the next section that the starburst population extends over a much smaller area, less than 1/6, than the ionized gas. Both the mean value and the spread of $[SII]/H\alpha$ increase for decreasing $H\alpha$ surface brightnesses (Figure 7, see Wang, Heckman & Lehnert 1998, Martin 1997, and Ferguson et al. 1996b on a variety of galaxies), supporting what is observed in Figure 6.

The reddening-corrected ionizing photon rate from the starburst is $\log Q(H^o)=52.57$ – 52.78 , depending on the dust opacity adopted for the central star cluster ($9 \text{ mag} \leq A_V \leq 35 \text{ mag}$, Calzetti et al. 1997). These values correspond to a Strömgren radius $R_S=240$ – 280 pc, for an electron density of 93 cm^{-3} and temperature $\sim 10,000$ K (Storchi-Bergman, Kinney & Challis 1995, CKS94), and for a filling factor of 0.01 (Martin 1997). The calculated Strömgren radius is at least a factor ~ 4.5 smaller than the extent of the $H\alpha$ emission.

3.2.3. The Morphology of ‘Shocks’ and DIG

Adopting arbitrarily the constraints $\log([OIII]/H\beta) > 0.2$ and $\log([SII]/H\alpha) > -0.35$ to discriminate between predominance of photoionization and predominance of shock excitation/hardening of radiation (or other mechanism), the location of the ‘shocked’ regions is graphically represented in Figure 3h. The figure shows that the purely photoionized region has a circularly symmetric shape centered almost exactly on the main ionizing cluster, with radius $\simeq 560$ pc; it is comparable in size to the stellar population of the starburst, although the morphology of the two is different (see next section). The ‘shocked’ gas has a markedly asymmetric morphology; the majority of the bins with $\log([OIII]/H\beta) > 0.2$ and $\log([SII]/H\alpha) > -0.35$ is located in the south-west region, and there appears to be an overlap of filaments and arches extending out of the main starburst area. The ‘shocked’ gas extends in the direction of the major axis of the galaxy; one would expect expanding gas to prefer the direction of the minor axis (e.g., Heckman et al. 1990, De Young & Heckman 1994, Martin 1998, Meurer, Staveley-Smith, & Killeen 1998), which does not seem to be true for NGC5253.

The constraint $\log([SII]/H\alpha) > -0.35$ corresponds to a $H\alpha$ surface brightness less than $6.39 \times 10^{-16} \text{ erg cm}^{-2} \text{ s}^{-1} \text{ arcsec}^{-2}$, or a normalized surface brightness $SB(H\alpha)/SB_e < 0.01$, in Figure 7. We stress again here that variations in the underlying stellar absorption would have typically no more than a 20% effect on both the $SB(H\alpha)$ and the $[SII]/H\alpha$ ratio (see Figure 3d). The ratio $SB(H\alpha)/SB_e < 0.01$ marks a sharp increase in the median value of $[SII]/H\alpha$. A similar

sharp break is evident also in the histogram of the bins with specific value of $H\alpha$ surface brightness (Figure 8): below $SB(H\alpha)/SB_e = 0.01$ there is a large gradient in the relative number of bins. Such “breaks” have been pointed out by Wang (1998) as the transition between HII regions and DIG. In the case of NGC5253, the DIG surrounds the central starburst up to a distance of at least $\sim 1.4\text{--}1.6$ kpc in some directions (to our detection limit).

3.2.4. *The Morphology of the Starburst Population*

In order to compare in detail the morphologies of the ionized gas and of the ionizing stars, we have removed the underlying galaxy from the broad band image, so that the structure of the current starburst would be enhanced.

The U band image includes the $[OII]\lambda 3727 \text{ \AA}$ doublet emission in its passband. In the central $15''$ $[OII]$ has $EW=130 \text{ \AA}$, thus providing about 20% contribution to the U emission. Since we did not observe the $[OII]$ emission, we used the $[SII]$ map, which was rescaled to the $[OII]$ intensity observed by Storchi-Bergmann et al. (1995). This procedure relies on the (reasonable) assumption that $[OII]$ and $[SII]$ have the same morphology and intensity distribution; this is supported by the observations of Martin (1997). The $H\alpha$ contribution to the R band image has been removed in a more straightforward manner (see section 2). All three broad band images were corrected for the effects of dust reddening using the HST reddening maps (or the constant value $E(B-V)=0.1$ outside the range of the HST maps) and the prescription of Calzetti et al. (1997).

The U-band isophotes external to $\sim 70''$ follow an exponential profile (Caldwell & Phillips 1989), typical of the old stellar populations in spheroidal and irregular dwarf galaxies. Indeed, NGC5253 would very likely be classified as a dwarf elliptical (Sersic et al. 1972) if it weren’t for the central starburst. At smaller radii there is a clear excess relative to the exponential fit; Caldwell & Phillips attribute this excess to the star formation event which occurred in the galaxy over the last ≈ 1 Gyr. Not all of this excess is composed of ionizing stars; along the galaxy major axis, the region between $50''$ and $70''$ is not associated with $H\alpha$ emission (to our detection limit). The ionizing starburst appears more concentrated than the population excess over the exponential light profile. To remove the non-ionizing stellar population underlying the ionizing starburst, we used the isophotes between $50''$ and $70''$, and attempted both an exponential profile and a $r^{1/4}$ law model. The latter fits the non-ionizing population isophotes to $r \sim 34''$ better than the exponential profile. This isophotal profile was extrapolated to the center and subtracted from the original image. The residual, namely the central starburst, is shown in Figure 3a for the U band. All three continuum images present the same morphology, thus hinting that dust extinction does not affect the global appearance in the optical passbands. The colors of the underlying galaxy are fairly uniform, with values $U-V=0.5\pm 0.2$ and $V-R=0.80\pm 0.25$, typical of a stellar population dominated by A7 and later type stars, which will not contribute to the photoionizing luminosity.

The comparison between the starburst continuum emission and any of the line emission or

line ratio maps shows an obvious characteristic: the line emission is more extended, by more than a factor ~ 2 , than the continuum emission (see Figure 3a with 3b). This is true for both the photoionized and shock-ionized parts of the nebular line emission, confirming that the photoionized gas is displaced relative to the ionizing stars by more than ~ 1 kpc from the external perimeter of the starburst. A plot of the $H\alpha$ surface brightness as a function of the $U-V$ color of the starburst population shows the expected trend that higher $SB(H\alpha)$ coincide on average with bluer $U-V$ colors (Figure 9). The regions with $SB(H\alpha)/SB_e > 0.01$ have typical colors $U-V \simeq -0.5, -1.3$, corresponding to ages between 1 and 100 Myr for constant star formation and between 1 and 30 Myr for an instantaneous burst population (Leitherer & Heckman 1995); this agrees with the age range found by Calzetti et al. (1997). A few points in this region have $U-V < -1.6$, bluer than the bluest models for stellar populations. This reflects uncertainties in the color derivation and, possibly, an imperfect subtraction of the strong [OII] emission from the U-band image. Lower $SB(H\alpha)$ correspond to regions with typical colors of nonionizing or mildly ionizing populations. We highlight again that the ionizing stellar population extends over an area which is $< 1/6$ of the area of the detected gas emission.

3.2.5. *Star Formation in the Dust Lane*

The values of $[OIII]/H\alpha$ along the dust lane (see the little ‘horn’ sticking out at the bottom left of Figure 3f) have median $\simeq 6$, compatible with the values in the center of the starburst. In addition, the ratio $[OIII]/[SII]$ remains high, around or above 10 (about 1/2 the value of the central cluster, see Figure 3g), along the entire dust lane. Insufficient reddening correction due to the presence of the dust lane would make both ratios even higher. This is one of the areas responsible for the marked spread in the $[OIII]/H\beta$ values at large distance from the center. We can place an upper limit $[SII]/H\alpha < 0.35$ in this area. Both line ratios are compatible with this region being almost purely photoionized. However, there are no obvious ionizing stars in this area, although we cannot exclude that star formation is heavily embedded in the dust lane, and thus is not visible. Even if this is the case, star formation in the lane is happening at a relatively low intensity level; the star-formation-sensitive $10 \mu\text{m}$ map of Telesco et al. (1993), indeed, does not show emission along the dust lane, and dust obscuration is less effective at $10 \mu\text{m}$ than in the optical.

3.3. NGC 5236

3.3.1. *Morphology of the Starburst*

The global morphology of the ionized gas emission in NGC5236 is far simpler than in NGC5253, and, likely, easier to interpret. Most of the $H\alpha + [NII]$ emission comes from the central $\sim 40''$, where the starburst is located, and along the spiral arms (Figure 2b). Unlike NGC5253,

there is little or no evidence for arcs, loops or filaments of ionized gas extending outward from the central starburst. In the center of the galaxy, the brightest part of the $H\alpha+[NII]$ emission, above 15σ , occupies a region $\sim 30''$ across (corresponding to a physical size of 540 pc), comparable in size and morphology to the bright blue stellar emission detected in the U band (above 50σ , Figures 4a and 4b). The optically brightest part of the starburst is located in the south-western arc of blue stellar clumps, about $15''$ in length. The northern tip of the arc appears to bend in the east direction, but this morphology probably is an effect of the crossing of the dust lane (see Gallais et al. 1991). The arc-shape of the stellar continuum is fairly well mirrored by the $H\alpha+[NII]$ emission, with no obvious exceptions. The ionized gas and blue star morphology of the center of NGC5236 is typical of the central starbursts hosted in massive galaxies, where rings, arcs, and “spirals” of star formation are common structures (Maoz et al. 1996, Colina et al. 1997). All characteristics of NGC5236, including those described below, are consistent with star formation occurring in a sharply bounded inner nuclear disk, perhaps defined by the inner Lindblad resonance (ILR) as suggested by Telesco et al. (1993).

Figure 4c displays the HST-WFPC1 image of the center of the galaxy in the F336W filter (Heap et al. 1993, roughly corresponding to the U-band), where the arc (‘A’ in Figure 4c) clearly splits into several individual stellar clusters and the northern ‘bend’ of the arc (‘B’ in Figure 4c) splits into three clusters. We cannot resolve the individual line emission of each of the clusters in ‘B’ from the ground-based image, but their summed flux locates the peak of $H\alpha+[NII]$ emission in the galaxy center, with a total observed flux $F(H\alpha+[NII])=1.40\times 10^{-12}$ erg s $^{-1}$ cm $^{-2}$, measured in an aperture of $2.6''$ diameter. The nucleus (‘N’ in Figure 4c) is located about $6''$ NE of the arc; it appears as a lump in the ground-based U-band image (Figure 4a), but with a weak $H\alpha+[NII]$ emission (Figure 4b).

About $11''$ North-West of the arc there are two bright HII knots (‘C’ and ‘D’ in Figure 4c; clump ‘D’ is not visible in the U-band image); they have comparable intensity in the narrow line emission, with the northern-most of the two (‘D’) being only 30% brighter than the other, but very different U brightnesses, with ‘D’ being 5.9 times fainter than the other. We identify ‘D’ as coincident with the mid-IR northern source (Telesco et al. 1993). The difference in line/continuum emission between the two knots is likely an age effect with ‘D’ being younger than ‘C’; if it were simply an effect of dust reddening ‘D’ would appear in near-IR imaging, but this is not the case (Gallais et al. 1991). The younger age of knot ‘D’ is supported by the value of the $H\alpha$ EW, which is about 180 \AA for this knot, while it is only about 90 \AA for knot ‘C’. Larger values of the $EW(H\alpha)$ locate comparatively younger regions (Leitherer & Heckman 1995); in the case of the center of NGC5236, an imaginary line joining region ‘B’ with knots ‘C’ and ‘D’ identifies the youngest part of the starburst, with values $EW(H\alpha)\approx 200 \text{ \AA}$ (Figure 4d), about twice those of surrounding regions (Telesco et al. 1993). The inferred ages from such EWs are less than 10^7 yr, for an instantaneous burst of star formation (Leitherer & Heckman 1995, see Puxley et al. 1997).

The three luminous condensations in the arc (‘A’ in Figure 4c, corresponding to multiple clusters in the HST image) are between 1.61 and 2.05 times brighter in U than clump ‘B’, while

they are a factor between 2.4 and 4.2 fainter in $H\alpha+[NII]$. In $[OIII]$, the features in arc ‘A’ are about 2.4 times brighter than ‘B’. If the metallicity along the arc is roughly constant, these differences are immediately understandable in terms of dust reddening, with ‘B’ being more reddened than ‘A’. This is reasonable as ‘B’ is located very close to the NS dust lane.

3.3.2. Gas Excitation

The $[OIII]\lambda 5007\text{\AA}/H\alpha$ ratio is plotted as a function of $[SII]\lambda\lambda 6717,6731\text{\AA}/H\alpha$ in Figure 10. Sokolowsky’s models, derived for cosmic abundances, are expected to work fairly well for this galaxy, whose center has average metallicity about twice solar. The data are not inconsistent with photoionization models, in the entire range considered. There is little evidence for shocks in NGC5236, although our line ratios cannot be used as the only criterion for deciding the ionization mechanism, because of the potential for heavy dust reddening effects in the $[OIII]/H\alpha$ ratio. The plot of $[SII]/H\alpha$ as a function of the distance from the $H\alpha$ peak (Figure 11a) also shows that photoionization appears to be the main gas excitation mechanism, as the trend of the upper envelope to the points closely follows Sokolowski’s model for depleted abundances. Further support to the photoionization picture comes from the range of values covered by the $[SII]/H\alpha$ ratio: it is very close to that measured in NGC5253, despite the fact that NGC5236 is at least one order of magnitude more metal-rich (cf. Figure 11a with 6a). The latter conclusion does not qualitatively change even if there is a 50% uncertainty in the stellar absorption underlying the $H\alpha$ emission or a similar uncertainty in the $[NII]$ contribution to the $H\alpha$ image.

The plot of the $[OIII]/H\alpha$ ratio as a function of the distance from the peak of the $H\alpha$ emission is instead fairly inconclusive (Figure 11b): here the scatter in the data points dominates any trend. The scatter in Figure 11b is likely the superposition of two effects: one is the inhomogeneity of the dust reddening, which we cannot correct for with our data, the other may be the lack of a correlation between the line ratio and the distance from the peak of the $H\alpha$ emission. The presence of the second effect is confirmed by Figure 11a. In this case variations in the reddening induce small changes in the line ratio; nevertheless, the plot still shows a fairly large scatter. The most straightforward interpretation is that the peak of the $H\alpha$ emission is not the absolute peak of the ionized gas emission. Unlike the case of NGC5253 (Figure 6 and discussion in Calzetti et al. 1997), the gas morphology in the center of NGC5236 cannot be described as the effect of a main central ionizing source, but is far more complex with multiple emission peaks of almost comparable intensity (see Figure 4b).

As in NGC5253, the largest values of the $[SII]/H\alpha$ ratio are reached in the regions of lowest $H\alpha$ surface brightness (Figure 12). Here, however, the scatter is much larger than in the case of NGC5253, probably due to the insufficient extinction correction of the $H\alpha$ surface brightness and uncertain correction for the underlying stellar absorption. Also, the $H\alpha$ surface brightness limit reached for NGC5236 is about 3 times higher than for NGC5253, due to shorter exposure times in both the 6563/78 and the R band filters, only partially compensated by the fact that the red

continuum of NGC5236 is about 5 times brighter than that of the other galaxy.

The histogram of the number of area bins having a specific value of the $H\alpha$ surface brightness (Figure 13) shows that the two galaxies have similar behavior (slope and upper limit) at the high brightness end, but differ quite substantially in the low surface brightness regime. In particular, NGC5236 does not show the ‘break’ in the power-law trend shown by NGC5253. Thus, the transition between HII regions and DIG is less clear in the spiral galaxy. Such variety of behaviors among galaxies has been previously observed (Wang, Heckman & Lehnert 1998).

The starburst population of NGC5236 is not easily separated from the underlying stellar population, because of the presence of uneven dust/stellar population distribution across the entire galaxy. The direct comparison of the U and $H\alpha$ images, discussed above (Figure 4, panels a-c), shows that the morphology of the blue stars closely follows that of the ionized gas. This suggests that the U-band image of the center of NGC5236 is tracing the optically detectable starburst population. Figure 14 shows the azimuthally-averaged profile of the surface brightness of both $H\alpha$ and U-band in annuli of increasing distance from the center. The two surface brightnesses have similar half-light radii, around $5''.5$, with profiles of almost identical shape. In both cases the assumption is that the emission of the underlying non-starburst stellar population is fairly constant out to $\sim 40''$ (see Figure 14). The almost identical values of the half-light radii also confirms that the gas emission in the center of NGC5236 is as extended as the starburst population, and there is no evidence for ‘leakage’ of ionized photons beyond the starburst region.

In summary, the characteristics of the nebular emission in the starbursting center of NGC5236 are typical of gas excited predominantly by photoionization. This conclusion should be regarded as preliminary, for the following three reasons: (1) the continuum-subtracted narrow-band images of NGC5236 are less deep than those of NGC5253, especially the crucial [OIII] image; (2) the contribution of the [NII] lines to the $H\alpha$ emission is almost 4 times higher in NGC5236 than in NGC5253; the impact of variations of the [NII]/ $H\alpha$ line ratio on the [SII]/ $H\alpha$ map is moderate if the [NII]/ $H\alpha$ changes by less than 50% but increases for larger variations; (3) we do not have appropriate information to correct for variations of the dust reddening across the central region. Our [OIII] maps of NGC5236 contain limited information despite the long exposure times (see Figure 4f). This is a consequence of the large metallicity in this galaxy: higher metallicities correspond to lower intensities for the O^{++} ion emission.

Incidentally, while [SII]/ $H\alpha$ has typical values in the range 0.15–0.4 in the Northern spiral arm of the galaxy, the ratio covers the range 0.2–1.4 and has a more extended cross section in the Southern spiral arm (Figure 2c). A difference between the two arms is evident neither from the stellar continuum morphology, nor from the colors. Since we cannot easily discriminate between dust reddening and age of the stellar population, a difference between the intrinsic stellar populations in the two arms cannot be excluded.

4. Discussion

The investigation of the morphology and physical conditions of the ionized gas in the galaxy pair NGC5253/NGC5236 demonstrates that the ionization structure is different in the two central starbursts, and probably reflects the morphological difference of the host galaxies. Both galaxies responded to a possibly common trigger with a large scale central starburst (size of order 500 pc), but the starburst in NGC5253 was probably more extended in the past (Caldwell & Phillips 1989). NGC5236 is also experiencing a somewhat milder event in its center, with a SFR about 1/3–1/4 that of NGC5253, although dust reddening corrections are uncertain. The major difference between the two starbursts appears to be, however, in their impact on the surrounding ISM, as discussed below.

4.1. NGC5253

4.1.1. *The Diffuse Ionized Medium*

The central concentration of the blue stars relative to the ionized gas seen in NGC5253 is typical of intense star-forming events, ranging from giant HII regions like 30 Dor or NGC604 (Kennicutt & Chu 1994, Muñoz-Tuñón 1994), to Blue Compact Dwarf galaxies (e.g., Meurer et al. 1992). The structure of the starburst in NGC5253 closely matches these expectations. The extended ionized gas emission is probably the manifestation of the hydrodynamic effects of radiation pressure and stellar winds/supernovae on the ISM surrounding the starburst, in combination with the photoionization effects of luminous sources. This conceptual model accounts for complex structures, like bubbles and filaments, in the low surface brightness $H\alpha$ emission. In terms of luminosity, the $H\alpha$ flux which is not directly associated with massive stars and, thus, can be associated with the DIG is 13% of the total. This fraction is for the projected emission only; we do not attempt to extrapolate it to the entire 3-dimensional distribution as this would require “guessing” the gas distribution along the line of sight. The locus of massive stars is defined as the region where the U-band emission from the starburst is detected (Figure 3a). Thus about one-tenth, and probably more, of the $H\alpha$ emission in NGC5253 is spatially separated from the source of ionization.

4.1.2. *The Contribution of Shocks and Other Processes*

The peripheral regions of the ionized emission in NGC5253 show the presence of a shock or other non-photoionization component in the gas excitation mechanism. Although the candidate shock structures we identify in the previous section (Figure 3h) need spectroscopic confirmation, it is clear that some contribution to the nebular line emission from non-photoionization (‘shock’) excitation needs to be present to explain the observed line ratios.

The morphology of the ‘shocked’ gas (Figure 3h) closely follows that of the bubbles South-West of the starburst center and the filaments in the Northern region. In particular, the bulk of the ‘shocked’ area is located at the position of the major-axis bubble, and extends in the direction of the finger of soft X-ray emission in the map of Martin & Kennicutt (1995) and along the axis of the X-ray emission detected by Strickland & Stevens (1999). The X-ray finger of Martin & Kennicutt extends for about $2'$ away from the galaxy center, not very different from the $1'.3$ scale of the ‘shocked’ region. A possibility therefore exists that the hot gas in overlapping superbubbles, which is most likely responsible for the extended X-ray emission (Strickland & Stevens 1999), also affects the optical emission line spectrum. Given the relatively low photon luminosity of the X-ray sources in NGC 5253 ($\leq 10^{44}$ photons $\text{cm}^{-2} \text{s}^{-1}$), the X-rays should make at modest contribution to the level of photoionization in most of NGC 5253. However, in addition to shocks within the hot bubbles (see Martin & Kennicutt 1995), there is the possibility that transition layers of warm, rapidly cooling gas exist within or on the boundaries of these regions. One example of this type of emission region are ‘turbulent mixing layers’, such as those described by Slavin, Shull, & Begelman (1993), which could become significant sources of emission in regions with low gas column densities. Emission line ratios from mixing layers can mimic shocks in the diagnostic emission line ratios which we have available, and this possibility therefore merits future examination. However, since hot ejecta from the central starburst can be responsible for shocking the outer regions of the DIG, we discuss below the viability of shocks to explain the observed line ratios.

A size scale of about $1'.3$ for the shocked region corresponds to a physical size of 1.45 kpc, which, for an expansion velocity of 35 km s^{-1} (Marlowe et al. 1995), corresponds to an age of 40 Myr for the bubble. Star formation within the central $\sim 300 \text{ pc}$ has been ongoing for $\sim 100 \text{ Myr}$, long enough to drive such a shock (Calzetti et al. 1997). The low velocity values observed by Marlowe et al. represent a potential difficulty for interpreting the ionization of this region as due to shocks. However, the line-of-sight velocity may not be representative of the expansion velocity of the bubble; if we adopt a shock velocity of 100 km/s , the age of the region decreases to $\sim 15 \text{ Myr}$.

The $\text{H}\alpha$ intensity associated with the shocked component is 2.2% of the total $\text{H}\alpha$ emission, after correction for underlying stellar absorption and dust obscuration (accounting only the area for which $[\text{SII}]/\text{H}\alpha$ is detected above 5σ , see Figure 3). This value is an upper limit, as the regions we define as ‘shocked’ can also be partially photoionized; we assume, conservatively, that only half, or 1.1%, of the ionized gas emission in the ‘shocked’ areas is actually excited by shocks. This fraction, however, does not include the fainter, more extended DIG, since here $[\text{SII}]$ is either undetected or is detected below our 5σ cut. Whichever the actual shocked $\text{H}\alpha$ emission fraction, it will still be a few percent at most. The $\text{H}\alpha$ flux associated with the shock is $3.2 \text{ E}-13 \text{ erg s}^{-1} \text{ cm}^{-2}$, corresponding to a luminosity of $6.1 \times 10^{38} \text{ erg s}^{-1}$ at the distance of NGC5253.

We can compare this value with the amount of mechanical energy input expected from the starburst. The reddening-corrected flux density at $2,600 \text{ \AA}$ from the star-forming region is

$F(2600)=4.5 \text{ E-13 erg s}^{-1} \text{ cm}^{-2} \text{ \AA}^{-1}$, corresponding to a luminosity of $\sim 8.6 \times 10^{38} \text{ erg s}^{-1} \text{ \AA}^{-1}$, from the data of Calzetti et al. (1997). This estimate does not take into account the fraction of massive stars so deeply buried in dust, e.g., along the dust lane, that their accounting is missing from the UV flux; a comparison between the optical nebular emission and the radio thermal emission (Beck et al. 1996) shows that the missing fraction amounts to $\approx 20\%$ of the reddening-corrected UV flux. Given the star formation history of the galaxy and the above UV flux, the mechanical energy being deposited into the ISM by massive stars is $\sim 8.5 \times 10^{40} \text{ erg s}^{-1}$ (Leitherer & Heckman 1995), a value very similar to what calculated by Marlowe et al. (1995) and by Martin & Kennicutt (1995). This energy rate is about 50% higher than the one derived for an expanding superbubble with the age and size given above and density of 12 cm^{-3} (Martin & Kennicutt 1995), using the self-similar solution of Weaver et al. (1977), and is more than sufficient to produce the observed X-ray luminosity (Strickland & Stevens 1999). About 2.5% of the shock input power is emitted in $\text{H}\alpha$ (Binette, Dopita & Tuohy 1985), implying that the gas shocked by the starburst in NGC5253 can produce a total luminosity $L(\text{H}\alpha) \sim 2.1 \times 10^{39} \text{ erg s}^{-1}$.

Most of the detected ‘shocked’ gas component is located in the south-western quadrant relative to a sphere centered on the main cluster. If the mechanical energy is emitted with bi-polar symmetry from the central starburst (Strickland & Stevens 1999), this quadrant is likely to receive $\approx 25\%$ of the total energy available to shocks, or $L(\text{H}\alpha) \sim 5.3 \times 10^{38} \text{ erg s}^{-1}$, comparable to the observed luminosity of $6.1 \times 10^{38} \text{ erg s}^{-1}$. The total mechanical energy available from the starburst can shock-excite gas to produce a total $\text{H}\alpha$ luminosity ~ 3.4 times what observed or about one-fourth of the 13% of $\text{H}\alpha$ emission we associate with the DIG. Observationally photoionization provides between 80% and 90% of the excitation of the DIG in NGC5253; this fraction is potentially lower, but not lower than $\sim 70\%$, even if all the mechanical energy were available to excite the gas.

Notably absent are shocks in the Eastern region; in section 3.2.5 we showed that the ionized gas associated with the dust lane in the E region is more consistent with photoionization rather than shocks (or other mechanism), even though local stellar ionizing sources have not yet been found. The absence of an obvious shock component here has another interpretation, possibly complementary to the previous one. The dust lane coincides with the position of the extremely weak CO detection in this galaxy (Turner et al. 1997). Turner et al. have interpreted the very low CO luminosity as evidence for the presence of extremely metal-poor gas in the area, possibly infalling gas which is feeding the central starburst. If the metallicity along the dust lane is lower than the average in the starburst, the $[\text{OIII}]/\text{H}\beta$ and the $[\text{SII}]/\text{H}\alpha$ ratios are expected to be higher and lower, respectively, than the average. Thus, presence of shocks along this region would go undetected by our method, as we are assuming a uniform metallicity for the ionized gas across the entire central region.

4.1.3. *The Structure of the Starburst*

Shocks in NGC5253 appear to have a preferential direction along the galaxy’s major axis. In addition the region along the dust lane, namely along the optical minor axis, appears dominated by photoionization. These facts, together with the HI kinematical data of Kobulnicky & Skillman (1995) and the CO detection of Turner et al. (1997) suggest the following picture for the starburst in NGC5253:

1. The central star formation is being fueled by gas which is either infalling along the minor axis, as suggested by Turner et al., or is located in a ‘disk’ rotating about the major axis, as suggested by Kobulnicky & Skillman on the basis of the HI rotation.
2. Hot ejecta from supernovae explosions and stellar winds drive the expansion of the ISM described in Martin & Kennicutt (1995) and in Strickland & Stevens (1999). The expansion is driven mostly in the direction perpendicular to the disk/infalling gas, where the gas density is lower (or, alternatively, is driven along the gas disk rotation axis). Hot ejecta from the central starburst, thus, shock the gas preferentially along the optical major axis. Also, the shocked gas is detected mainly along the south-western side of the major axis; the propagation of the northward shocks may be prevented by the high density region of the infalling-gas/rotating-gas-disk, which is located in the northern side of the star forming site.

This general picture is rather different from the one found for other dwarf galaxies by Marlowe et al. (1995), where the location of bubbles is preferentially along the optical minor axis, suggesting that the ionized gas expands mainly in the direction perpendicular to the plane of the galaxy. One can speculate that past interaction with NGC5236 played a role in the geometry of NGC5253; the massive ‘companion’ is located in the NW quadrant, at position angle P.A. $\sim -20^\circ$. This direction is only $\sim 25^\circ$ away from the minor axis and almost orthogonal, just $\sim 15-20^\circ$ away, to the direction of the shocked gas. Thus, the direction along which the encounter between the two galaxies happened may have determined the initial gas infall and subsequent gas expansion directions in NGC5253.

4.2. NGC5236

For NGC5236, the gas morphology allows a more straightforward interpretation than in NGC5253, although our conclusions are limited by the shallowness of the [OIII] map and by presence of large amount of dust in combination with the lack of an $H\beta$ image to perform dust reddening corrections. The $H\alpha$ emission correlates fairly well with the blue emission from the ionizing stars, and there is no evidence for extended ionized gas emission. The strong spatial overlap between blue stars and ionized gas indicates that we are not seeing any ‘bonafide’ DIG in the center of this galaxy; rather, ionization appears to be a local process. The [SII]/ $H\alpha$ values fall

into the photoionization range even after allowing for large uncertainties in the underlying stellar absorption and in the [NII] contribution, suggesting very little, if any, contribution from a shock or other non-photoionization component.

The central starburst in NGC5236 is a milder perturbation on its giant spiral galaxy host than the one in NGC5253. The past encounter with NGC5253 may have produced a stellar bar and/or triggered the gas inflow towards the center along the bar. The presence of an inner Lindblad resonance (Telesco et al. 1993) is the additional ingredient needed to produce a ring starburst (Shlosman, Begelman & Frank 1990). The absence of a shocked component in the ionized gas can be interpreted as an effect of the deep potential well in the center of NGC5236. The more massive the galaxy, the harder it is to disrupt the gas disk, especially in a high density center (De Young & Heckman 1994, MacLow & Ferrara 1998). In NGC5236, the mechanical energy being deposited into the ISM by the central starburst is $\approx 2 \times 10^{40}$ erg s⁻¹. This amount of power is probably inadequate to disrupt the ISM in the dense nuclear disk of NGC5236. The higher gas densities limit the growth of superbubbles, while the larger gravitational forces make expansion out of the plane more difficult. The calculations of De Young & Heckman refer to disruption along the minor axis, while we are looking at ISM expansion parallel to the gas disk (NGC5236 is seen nearly face-on). However, if the ISM is left intact along the minor axis, it is even more likely to remain confined in the center of the disk. Lack of obvious filamentary structures, bubbles and superbubbles in the ionized gas of NGC5236 fits in this picture.

5. Conclusions

The analysis of the starburst galaxy ‘odd couple’ NGC5253 and NGC5236 reveals very different ionized gas morphologies. The metal-poor, dwarf member of the pair, NGC5253, has the DIG emission typical of intense bursts of star formation, that accounts for about 13% of the projected H α luminosity. A small (~ 10 –20%), but not negligible, fraction of the DIG is ionized by shocks or other non-photoionization mechanism; this implies that between 80% and 90% of the H α emission from the DIG is due to photoionization from massive stars. The morphology of the ‘shocked’ gas is quite peculiar, as it extends along the optical major axis, orthogonal to the direction from which presumably the gas is feeding the central starburst. If the ‘shocked’ gas corresponds to one or more expanding bubbles driven by the central starburst, the in-plane morphology indicates that the metals ejected from the central region will remain inside the galaxy, and will not be lost in the intergalactic medium (Mac Low & Ferrara 1998). Photoionization of the DIG from massive stars means that about 10% of the ionizing photons are escaping from the central starburst zone.

In the metal-rich, grand-design spiral member of the pair, NGC5236, there is no clear detection of a DIG component in the starbursting nuclear region and the ionized gas does not show an obvious shocked component. This is probably because the gas is confined to the center by the deep potential well of the galaxy, and remains near the massive stars responsible for its

photoionization.

The fraction of DIG to total ionized gas in both starbursts is much smaller, probably due to projection effects, than the 20–50% measured in less active star-forming galaxies (Ferguson et al. 1996a, Wang et al. 1997, 1998). Although we can only place a lower limit to the amount of DIG in the two starbursts, it is unlikely that the actual fraction will be higher than what has been observed in other galaxies.

D.C., C.J.C., and A.L.K. thank the Carnegie Observatories for the hospitality and for granting them observing time at the Las Campanas Observatory. D.C. thanks Crystal Martin for useful discussions and suggestions during the analysis of the images. Part of this manuscript was written at the Kitt Peak 2.1-m telescope, during a stormy night.

Table 1. Summary of Filters, Calibrations, Limiting Sensitivities.

Filter	λ_c^a (Å)	FWHM (Å)	Flux Conversion ^b (erg cm ⁻² Å ⁻¹ ADU ⁻¹)	Detection Limit ^c
Harris U			2.139 E–18 (5%)	4.6 E–20
Harris V			2.550 E–19 (2%)	4.3 E–20
Harris R			1.160 E–19 (1.5%)	3.6 E–20
5000/70	4994	77	4.697 E–18 (4%)	7.4 E–18
6563/78	6568	68	2.361 E–18 (3%)	8.0 E–18
6737/76	6747	91	1.796 E–18 (3%)	9.3 E–18

^aThe central wavelength of the narrow band filters.

^bThe flux zeropoint is given with, in parenthesis, the internal uncertainty.

^cThe limiting surface brightness is in erg s cm⁻² arcsec⁻² for the continuum-subtracted narrow band images ([OIII], H α , and [SII]) and it is a surface brightness density in erg s cm⁻² arcsec⁻² Å⁻¹ for the broad band images. The values refer to 1 σ detection limits of the deepest images obtained in this project (see Table 2), rebinned to a resolution of 1".3, namely 5 \times 5 pix².

Table 2. Summary of Exposure Times.

Filter	NGC5253 Exp. Time ^a (s)	NGC5253 Exp. Time ^a (s)	NGC5236 Exp. Time ^a (s)	NGC5236 Exp. Time ^a (s)
Harris U	900.	8400.	210.	4500.
Harris V	120.	1200.	190.	920.
Harris R	240.	1520.	260.	...
5000/70	180.	10200.	870.	3000.
6563/78	240.	3900.	780.	1440.
6737/76	12000.	...	1560.	3840.

^aThe second and fourth columns are the total exposure times of the final unsaturated image for NGC5253 and NGC5236, respectively; the third and fifth columns are the total exposure times of the final images which have the central $\sim 5''$ – $20''$ of the galaxies saturated. Each unsaturated/saturated image is the combination of multiple exposures in the range 30–1200 s.

REFERENCES

- Aitken, D. K., Roche, P. F., Allen, M. C., & Phillips, M. M., 1982, *MNRAS*, 199, 31P
- Beck, S. C., Turner, J. L., Ho, P. T., Lacy, J. H., & Kelly, D. M. 1996, *ApJ*, 457, 610
- Binette, L., Dopita, M.A., & Tuohy, I.R. 1985, *ApJ*, 297, 476
- Bohlin, R.C., Cornett, R.H., Hill, J.K., Smith, A.M., & Stecher, T.P. 1983, *ApJ*, 274, L53
- Burstein, D., & Heiles, C. 1982, *AJ*, 87, 1165
- Caldwell, N., & Phillips, M. M. 1989, *ApJ*, 338, 789
- Calzetti, D., Meurer, G.R., Bohlin, R.C., Garnett, D.R., Kinney, A.L., Leitherer, C., & Storchi-Bergmann, T. 1997, *AJ*, 114, 1834
- Calzetti, D., Kinney, A.L., & Storchi-Bergmann, T. 1994, *ApJ*, 429, 582
- Chu, Y.-H., & Kennicutt, R.C. 1994, *ApJ*, 425, 720
- Colina, L., García Vargas, M.L., Mass-Hesse, J.M., Alberdi, A., & Krabbe, A. 1997, *ApJ*, 484, L41
- Crowther, P.A., Beck, S.C., Willis, A.J., Conti, P.S., Morris, P.W., & Sutherland, R.S. 1998, *MNRAS*, in press (astro-ph/9812080)
- De Young, D.S., & Heckman, T.M. 1994, *ApJ*, 431, 598
- Domgörgen, H. & Mathis, J. S. 1994, *ApJ*, 428, 647
- Dove, J.B., & Shull, J.M. 1994, *ApJ*, 430, 222
- Ehle, M., Pietsch, W., Beck, R., & Klein, U. 1998, *A&A*, 329, 39
- Elmegreen, B. G. 1992, in *Star Formation in Stellar Systems*, eds. G. Tenorio-Tagle, M. Prieto, F. Sánchez (Cambridge: Cambridge University Press), 383
- Elmegreen, B.G., & Lada, C.J. 1977, *ApJ*, 214, 725
- Ferguson, A.M.N., Wyse, R.F.G., Gallagher, J.S., & Hunter, D.A. 1996a, *AJ*, 111, 2265
- Ferguson, A.M.N., Wyse, R.F.G., & Gallagher, J.S. 1996b, *AJ*, 112, 2567
- Ferland, G.J. 1993, Internal Report, Dept. of Phys. & Astron., Univ. Kentucky
- Gallagher, J. S. & Hunter, D. A. 1990, *ApJ*, 362, 480
- Gallais, P., Rouan, D., Lacombe, F., Tiphene, D., & Vauglin, I. 1991, *A&A*, 243, 309
- Haffner, L.M., Reynolds, R.J., & Tufte, S.L. 1999, *ApJ*, accepted (astro-ph/9904143)

- Hamuy, M., Suntzeff, N.B., Heathcote, S.R., Walker, A.R., Gigoux, P., & Phillips, M.M. 1994, *PASP*, 106, 566
- Heap, S.R., Holbrook, J., Malumuth, E., Shore, S., & Waller, W. 1993, *BAAS*, 25, 840
- Heckman, T.M. 1997, in *Star Formation Near and Far, the 7th Annual Astrophysics Conference in Maryland*, S.S. Holt & L.G. Mundy eds. (Woodbury: AIP) 393, 271
- Heckman, T.M., Armus, L., & Miley, G.K. 1990, *ApJS*, 74, 833
- Hunter, D.A. 1994, *AJ*, 107, 565
- Hunter, D.A., & Gallagher, J.S. 1992 *ApJ*, 391, L9
- Hunter, D.A., & Gallagher, J.S. 1997 *ApJ*, 475, 65
- Kennicutt, R.C., 1989, *ApJ*, 344, 685
- Kennicutt, R.C., & Chu, Y.-H. 1994, in *Violent Star Formation*, ed. G. Tenorio-Tagle (Cambridge: Cambridge University Press), 1
- Kennicutt, R. C., Edgar, B. K. & Hodge, P. W. 1989, *ApJ*, 337, 761
- Kennicutt, R.C., & Hodge, P.W. 1986, *ApJ*, 306, 130
- Kinney, A.L., Bohlin, R.C., Calzetti, D., Panagia, N., & Wyse, R.F.G. 1993, *ApJS*, 86, 5
- Kobulnicky, H. A., & Skillman, E. D., 1995, *ApJ*, 454, L121
- Kobulnicky, H.A., Skillman, E.D., Roy, J.-R., Walsh, J.R., & Rosa, M.R. 1997, *ApJ*, 477, 679
- Lehnert, M.D., & Heckman, T.M. 1995, *ApJS*, 97, 89
- Leitherer, C., & Heckman, T.M. 1995, *ApJS*, 98, 9
- MacLow, M.-M., & Ferrara, A. 1998, in *The Magellanic Clouds and Other Dwarf Galaxies*, eds. T. Richtler and J.M. Braun (Aachen: Shaker Verlag), 177
- Maoz, D., Barth, A.J., Sternberg, A., Filippenko, A.V., Ho, L.C., Macchetto, F.D., Rix, H.-W., & Schneider, D.P. 1996, *AJ*, 111, 2248
- Marlowe, A.T., Heckman, T.M., Wyse, R.F.G. & Schommer, R. 1995, *ApJ*, 438, 563
- Martin, C.L. 1997, *ApJ*, 491, 561
- Martin, C.L. 1998, *ApJ*, 506, 222
- Martin, C. L., & Kennicutt, R. C. 1995, *ApJ*, 447, 171
- McCall, M. L., Rybski, P. M., & Shields, G. A. 1985, *ApJS*, 57, 1

- McCray, R., & Kafatos, M. 1987, *ApJ*, 317, 190
- Meurer, G.R., Freeman, K.C., Dopita, M.A., & Cacciari, C. 1992, *AJ*, 103, 60
- Meurer, G. R., Heckman, T.M., Lehnert, M.D., Leitherer, C., & Lowenthal, J. 1997, *AJ*, 114, 54
- Meurer, G., Staveley-Smith, L., & Killeen, N. E. B. 1998, *MNRAS*, 300, 705
- Monnet, G. 1971, *A&A*, 10, 467
- Muñoz-Tuñon, C. 1994, in *Violent Star Formation*, ed. G. Tenorio-Tagle (Cambridge: Cambridge University Press), 25
- Parker, J.W., Garmany, C.D., Massey, P., & Walborn, N.R. 1992, *AJ*, 103, 1205
- Petitpas, G.R., & Wilson, C.D. 1998, *ApJ*, 503, 219
- Puxley, P.J., Doyon, R., & Ward, M.J. 1997, *ApJ*, 476, 120
- Rand, R.J. 1998, *PASA*, 15, 106
- Reynolds, R.J. 1991, *ApJ*, 372, L17
- Rogstad, D. H., Lockhart, I. A., & Wright, M. C. H. 1974, *ApJ*, 193, 309
- Rouan, D., Tiphene, D., Lacombe, F., Boulade, O., Clavel, J., Gallais, P., Metcalfe, L., Pollock, A., & Siebenmorgen, R. 1996, *A&A*, 315, L141
- Sandage, A., Saha, A., Tamman, G. A., Labhardt, L., Schweneler, H., Panagia, N., & Macchetto, F. D. 1994, *ApJ*, 423, L13
- Satyapal, S., Watson, D.M., Pipher, J.L., Forrest, W.J., et al. 1997, *ApJ*, 483, 148
- Sérsic, J. L., Carranza, G., & Pastoriza, M. 1972, *Ap&SS*, 19, 469
- [Shlosman, I., Begelman, M.C., & Frank, J. 1990, *Nature*, 345, 679
- Shull, J.M. 1993, in *Massive Stars: Their Lives in the Interstellar Medium*, ed. J. P. Cassinelli & E. B. Churchwell (San Francisco: ASP), 327
- Shull, J.M., & McKee, C.F. 1979, *ApJ*, 227, 131
- Silk, J. 1997, *ApJ*, 481, 703
- Sivan, J.-P., Stasinska, G., & Lequeux, J. 1986, *A&A*, 158, 279
- Slavin, J. D., Shull, J. M., & Begelman, M. C. 1993, *ApJ*, 407, 83
- Sokolowski, J. 1993, private communication

- Storchi-Bergmann, T., Kinney, A.L., & Challis, P. 1995, *ApJS*, 98, 103
- Strickland, D.K., & Stevens, I.R. 1999, *MNRAS*, in press (astroph/9902188)
- Telesco, C. M., Dressel, L. L., & Wolstencroft, R. D. 1993, *ApJ*, 414, 120
- Trinchieri, G., Fabbiano, G., & Paulumbo, G.G.C. 1985, *ApJ*, 290, 96
- Turner, J. L., Beck, S. C., & Hurt, R. L. 1997, *ApJ*, 474, L11
- Turner, J. L., & Ho, P.T.P. 1994, *ApJ*, 421, 122
- Turner, J. L., Ho, P.T.P. & Beck, S. C. 1998, *AJ*, 116, 1212
- van den Bergh, S. 1980, *PASP*, 92, 122
- Walsh, J. R., & Roy, Roy, J.-R. 1989, *MNRAS*, 239, 297
- Wang, J. 1998, Ph.D. Thesis (The Johns Hopkins University)
- Wang, J., Heckman, T.M., & Lehnert, M.D. 1997, *ApJ*, 491, 114
- Wang, J., Heckman, T.M., & Lehnert, M.D. 1998, *ApJ*, 509, 93
- Wang, J., Heckman, T.M., & Lehnert, M.D. 1999, *ApJ*, in press (astroph/9811100)
- Weaver, R., McCray, R., Castor, J., Shapiro, P., Moore, R. 1977, *ApJ*, 218, 377

Fig. 1.— (Available as JPG file) The comparison of the R band (top panel) and the continuum-subtracted $H\alpha+[NII]$ (bottom panel) images of NGC5253 shows the extent of the ionized gas emission. North is up and East is left. Arcs and filaments of ionized gas are evident especially in the South-West region. Each image covers a field of view of $3'.36$ in side. Both images are among the deepest in our set and their central few arcseconds are saturated.

Fig. 2.— (Available as JPG file) The R band (panel a) and the continuum-subtracted $H\alpha+[NII]$ (panel b) images of NGC5236 are shown together with the $[SII]\lambda\lambda 6717,6731 \text{ \AA}/H\alpha$ line ratio map (panel c). Here the $H\alpha+[NII]$ emission runs along the two spiral arms departing from the center of the galaxy. Unlike the other galaxy, the ionized gas emission in NGC5236 shows little evidence for presence of arcs, filaments, or other complex structures. The $[SII]/H\alpha$ line ratio image also traces the central burst of star formation and the star-forming spiral arms. The grey scale in panel (c) marks values from a minimum of $[SII]/H\alpha \simeq 0.1$ (light grey) up to $[SII]/H\alpha \simeq 1.5$ (dark grey/black). The third panel has been resampled to $5 \text{ pix} \times 5 \text{ pix}$ bins. North is up and East is left. Each image covers a field of view of $5'.20$ in side.

Fig. 3.— (Available as JPG file) The deepest of our U-band images shows the full extent of the central starburst in NGC5253 (panel a) after subtraction of the underlying galaxy. North is up and East is left. Similar morphology and size are observed in the V and R band images. The central few pixels of the U image are saturated and, thus, masked out. The $H\alpha$ image (panel b) shows that the ionized gas emission extends beyond the region occupied by the massive star population of the starburst. In both panels (a) and (b) a darker shade means a higher surface brightness. The $H\alpha$ equivalent width (EW) (panel d) covers the range 10 \AA , at the edges of the detected ionized region (light grey), to $\sim 1,000 \text{ \AA}$, in the center of the starburst (dark grey). The $[SII]\lambda\lambda 6717,6731 \text{ \AA}/H\alpha$ is shown in panel (c), while the $[OIII]\lambda 5007 \text{ \AA}/H\beta$ and the $[OIII]\lambda 5007 \text{ \AA}/H\alpha$ line ratio images are in panels (e) and (f), respectively. The ionization map $[OIII]/[SII]$ is shown in panel (g). In these four panels, a darker shade means a higher value of the line ratio. The last panel (panel h) shows in black the location of those regions with $\log([OIII]/H\beta) > 0.2$ and $\log([SII]/H\alpha) > -0.35$, i.e. areas whose line ratios indicate presence of shocks or other non-photoionization mechanism. Each image is $2'.58 \times 2'.58$.

Fig. 4.— (Available as JPG file) The ground-based U-band image of the central $66'' \times 66''$ in NGC5236 (panel a) is shown together with the HST WFPC1 image obtained in the F336W filter (panel c). In neither case the continuum emission from the underlying galaxy has been subtracted. North is up and East is left. The labels in panel (c) correspond to a number of active regions of star formation described in the text. The U-band emission matches the extent of the $H\alpha$ emission (panel b) in the center of this galaxy. Panel (d) shows the $H\alpha$ EW map of the center of the galaxy, with values from $\sim 3-4 \text{ \AA}$ (light grey) up to $> 200 \text{ \AA}$ (dark grey). The $[SII]\lambda\lambda 6717,6731 \text{ \AA}/H\alpha$ and $[OIII]\lambda 5007 \text{ \AA}/H\alpha$ line ratio images are shown in panels (e) and (f), respectively. Grey-scale coding is as in Figure 3.

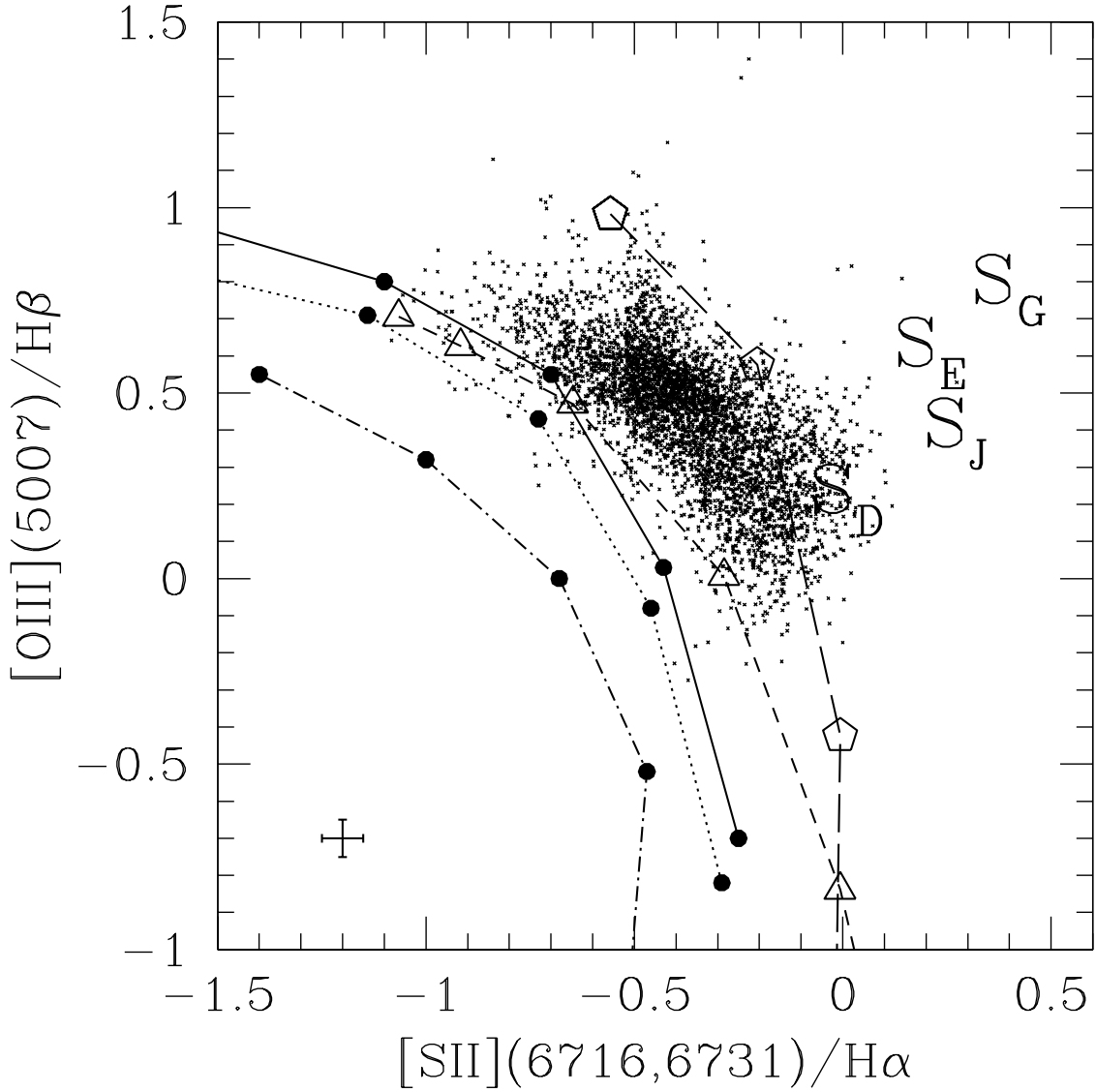


Fig. 5a.— (Panel a) The line ratios $\log([\text{OIII}]/\text{H}\beta)$ versus $\log([\text{SII}]/\text{H}\alpha)$ are shown for the central ~ 2.4 (diameter) of NGC5253; each data point (small crosses) represents a bin $1''.3$ in side, and has been corrected for both dust reddening and underlying stellar absorption. A representative 1σ error bar is shown at the bottom-left corner of the Panel. Predictions from a number of photoionization (Martin 1997, Sokolowski 1993) and shock (Shull & McKee 1979) models are also shown. Photoionization models locate the trend of line ratios for varying ionization parameter U . The filled circles give the models of Martin (1997), who run CLOUDY for a range of metal abundances ($[\text{O}/\text{H}]$) and effective temperature (T_e) of the central ionizing source. Here we report: $[\text{O}/\text{H}]=0.2 [\text{O}/\text{H}]_\odot$ and $T_e=50,000$ K (continuous line), $[\text{O}/\text{H}]=0.2 [\text{O}/\text{H}]_\odot$ and $T_e=45,000$ K (dotted line), and $[\text{O}/\text{H}]=1.0 [\text{O}/\text{H}]_\odot$ and $T_e=50,000$ K (dot-dashed line). From left to right, the filled circles indicate values of $\log(U)=-1.91, -2.58, -3.24, -3.92, -4.60$ for the sub-solar case, and $\log(U)=-1.73, -2.40, -3.08, -3.78, -4.60$ for the solar metallicity case. The Sokolowski's (1993) models show the line ratio locus in the case of depleted metal abundances (empty triangles and short-dashed line) and of a $5\times$ hardened radiation continuum (empty pentagons and long-dashed line). The models use cosmic abundances and stellar continuum generated by a Salpeter stellar mass function up to $120 M_\odot$. From left to right, the empty triangles (depleted abundances) identify values of $\log(U)=-2.00, -2.22, -2.58, -3.24, -3.92, -4.60$ and the empty pentagons (hardened radiation) $\log(U)=-2.58, -3.24, -3.92, -4.60$. The location of the line ratio predictions from shock models is indicated by capital "S". S_D , S_E , and S_G indicate shocks with cosmic abundance, gas density of 10 cm^{-3} and velocities $v=90, 100$, and 130 km/s . S_J indicates depleted abundances and $v=100 \text{ km/s}$.

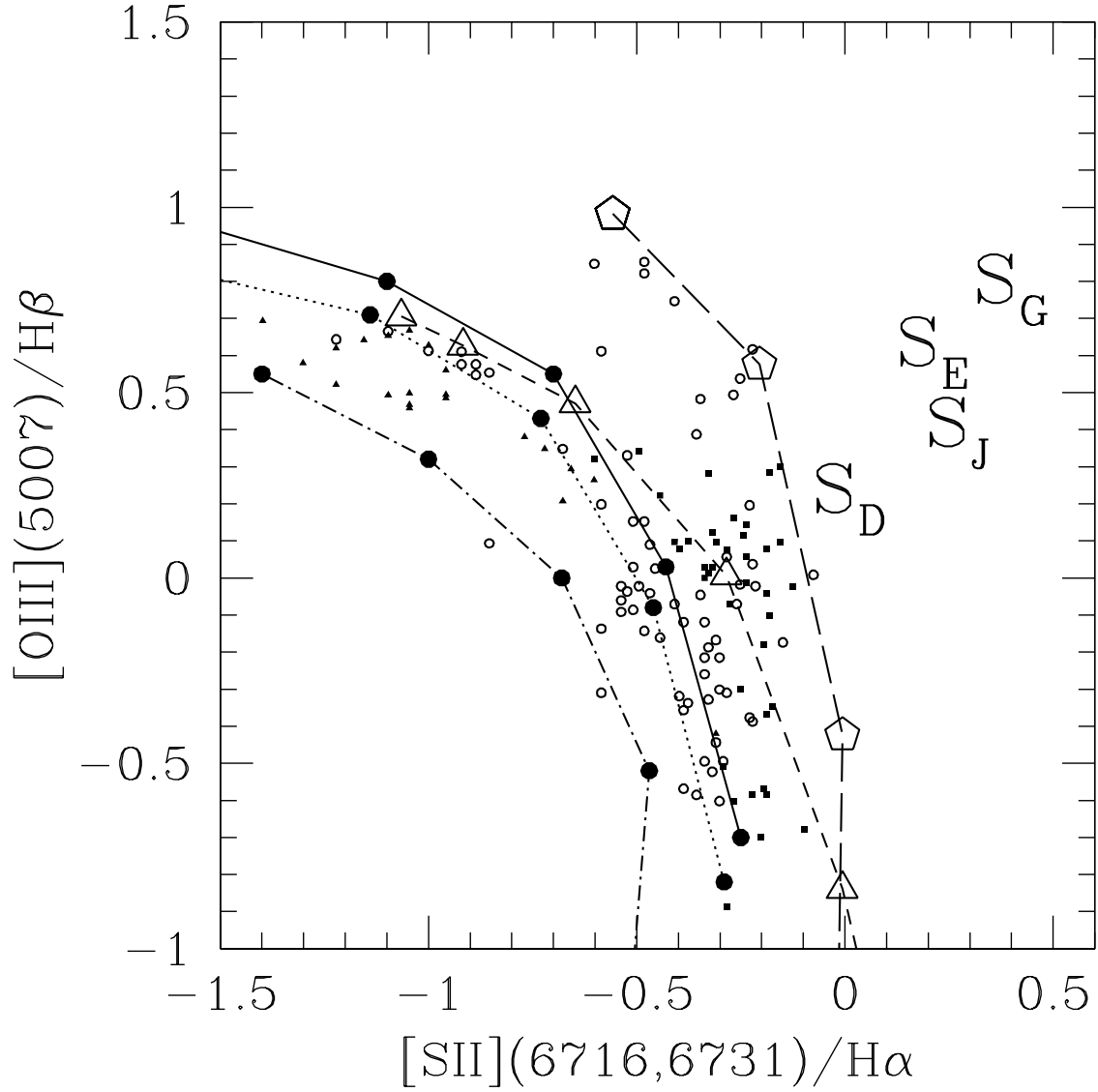


Fig. 5b.— (Panel b) The same as Panel (a), where the data points are relative to ionized gas emission in the Large Magellanic Cloud, from Hunter (1994). The symbols refer to HII regions (filled triangles), giant shells (empty circles) and super-shells (filled squares).

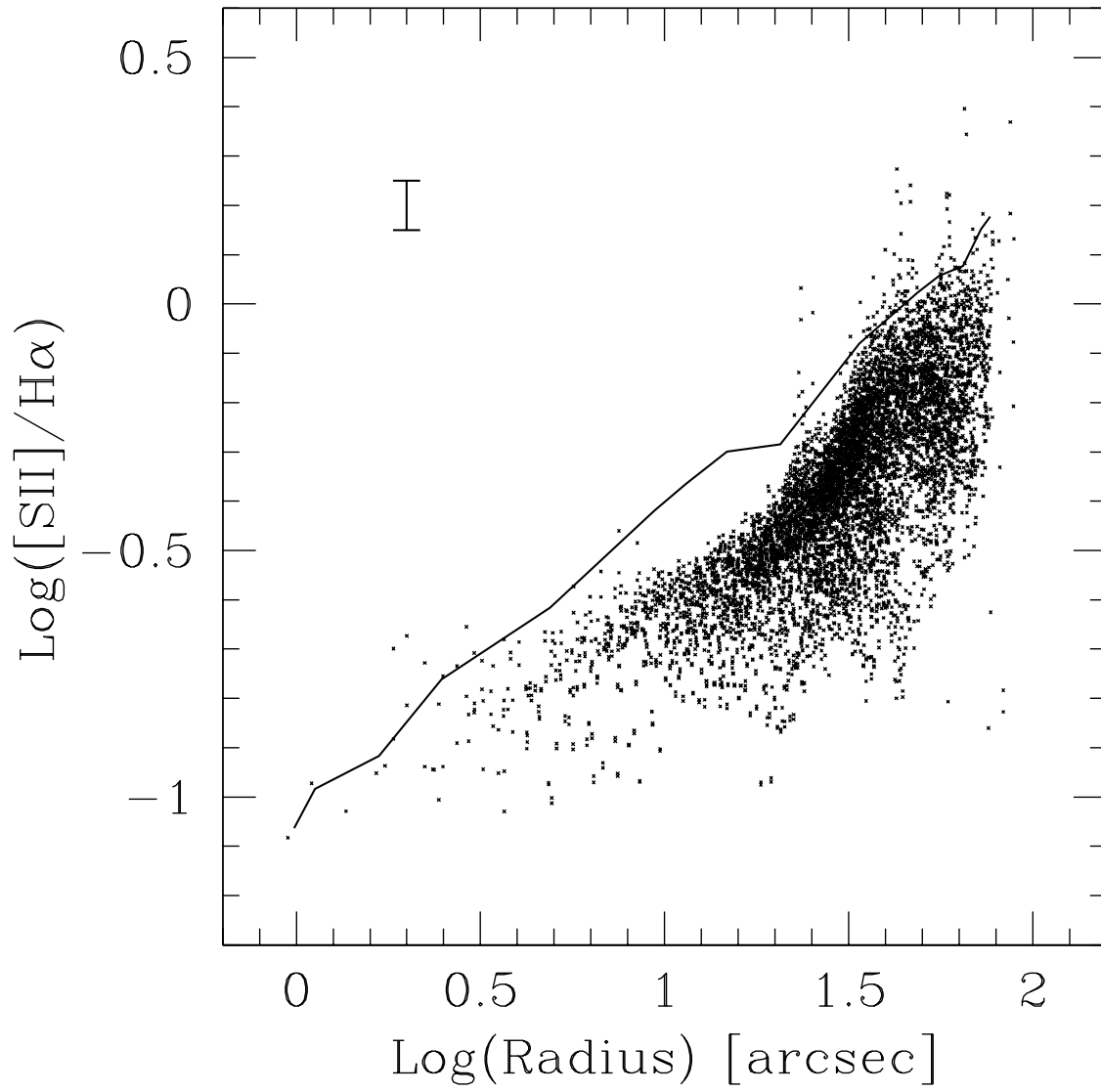


Fig. 6a.— (see next page for caption)

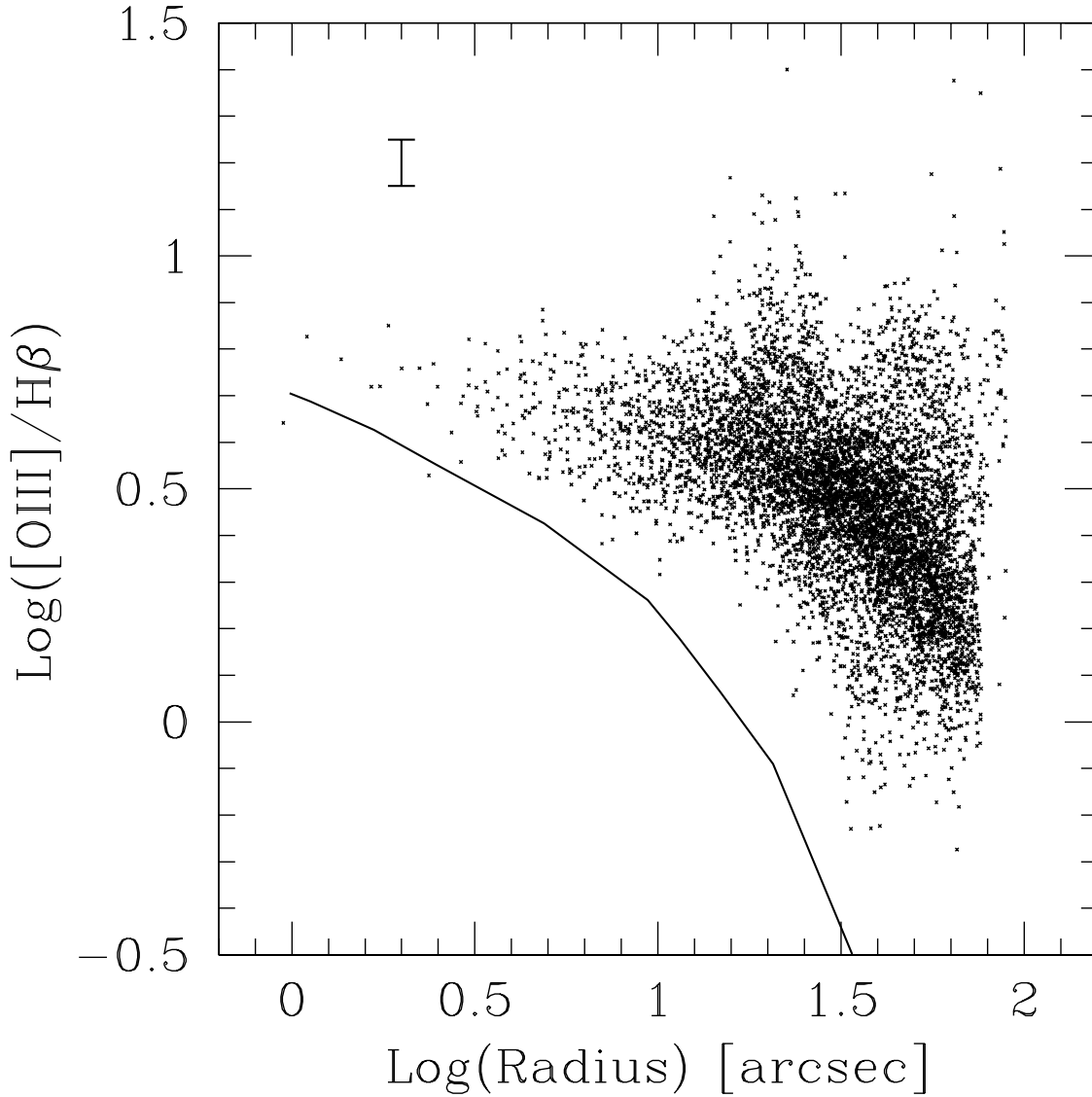


Fig. 6b.— The line ratios $[\text{SII}]/\text{H}\alpha$ (Fig. 6a) and $[\text{OIII}]/\text{H}\beta$ (Fig. 6b) are plotted as a function of the distance from the central star cluster in the NGC5253 starburst. Representative 1σ error bars are shown at the top-left corner of the Panels. The most distant regions are located ~ 1.7 kpc from the center. The continuous lines show the loci of the Sokolowski’s (1993) photoionization model with depleted abundances.

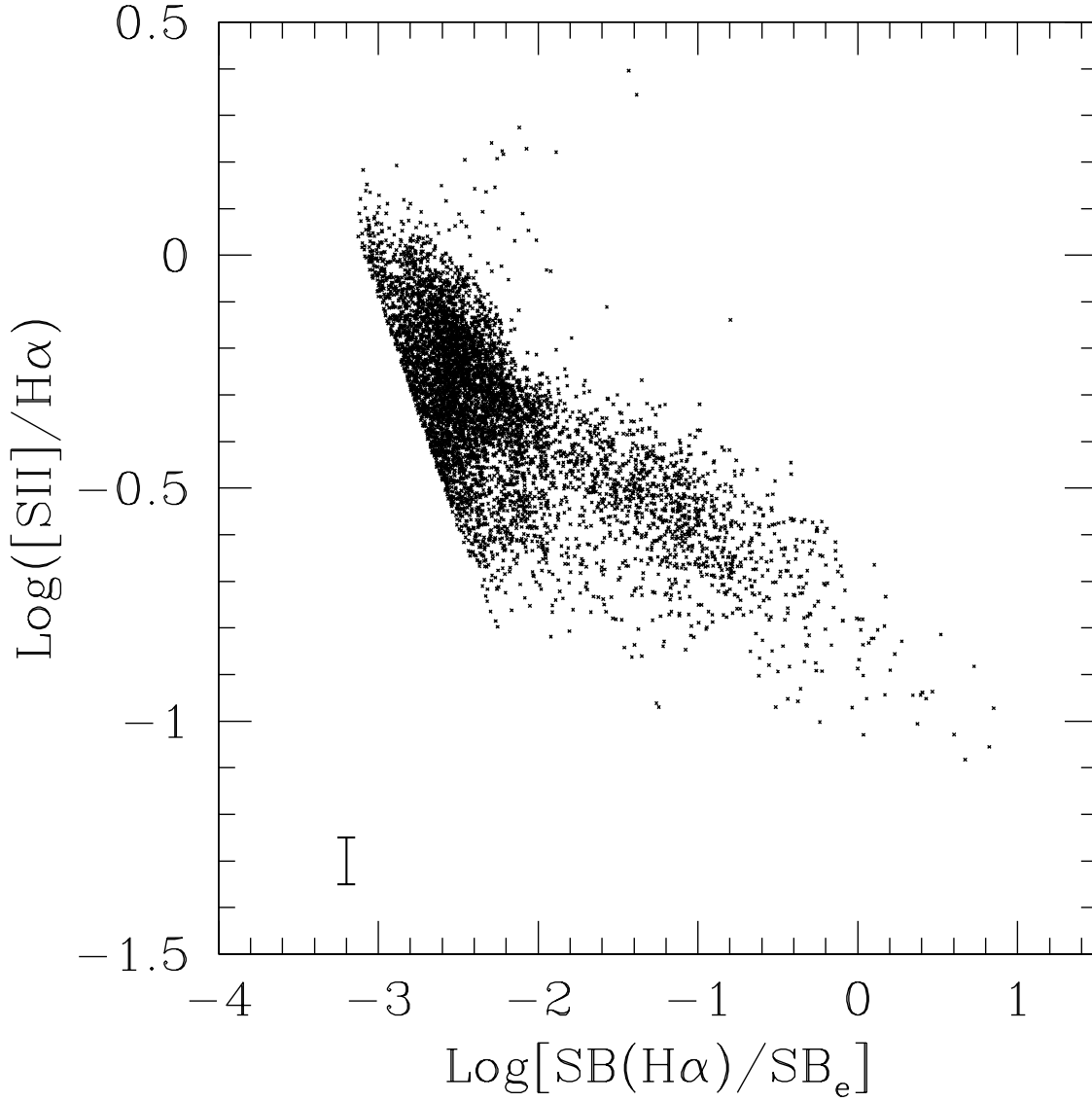


Fig. 7.— The line ratio $\log([\text{SII}]/\text{H}\alpha)$ as a function of the $\text{H}\alpha$ surface brightness for NGC5253. The $\text{H}\alpha$ surface brightness is normalized to the half-light radius surface brightness. A representative 1σ error bar is shown at the bottom-left corner of the Figure. The mean value of $[\text{SII}]/\text{H}\alpha$ decreases for increasing values of the $\text{H}\alpha$ surface brightness, as already observed in a variety of galaxies. The sharp cut on the data on the left hand side of the plot corresponds to the 5σ detection limit on both the line ratio and the $\text{H}\alpha$ surface brightness.

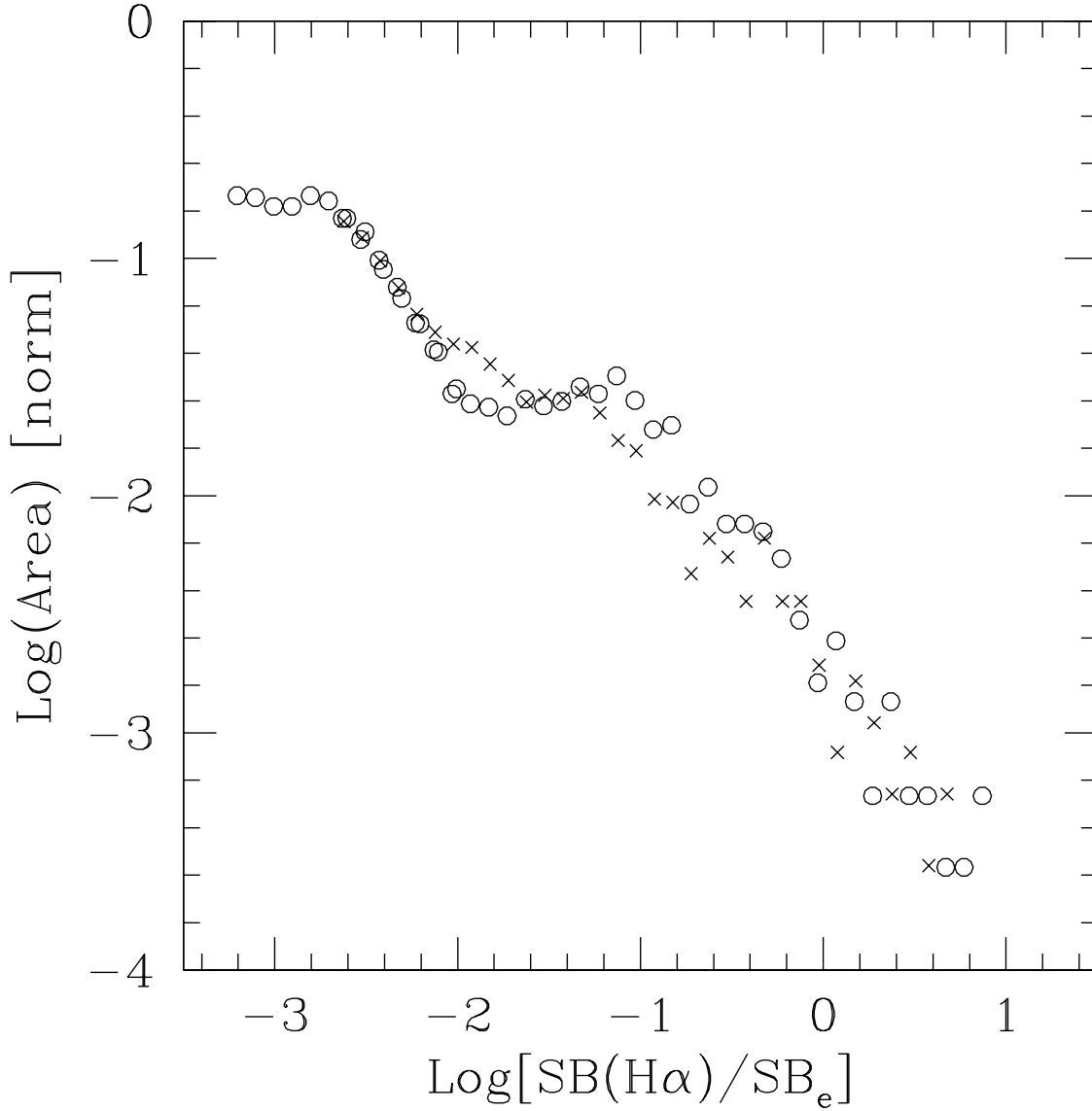


Fig. 8.— The histogram of the number of bins having a given value of the $H\alpha$ surface brightness as a function of the surface brightness itself, in NGC5253. The total area occupied by the bins is normalized to unity. The $H\alpha$ surface brightness is normalized to the mean half-light radius surface brightness. Values are reported for the surface brightness corrected for the underlying stellar absorption only (crosses) and corrected for both underlying stellar absorption and dust reddening (circles). A “natural” break occurs around $SB(H\alpha)/SB_e=0.01$.

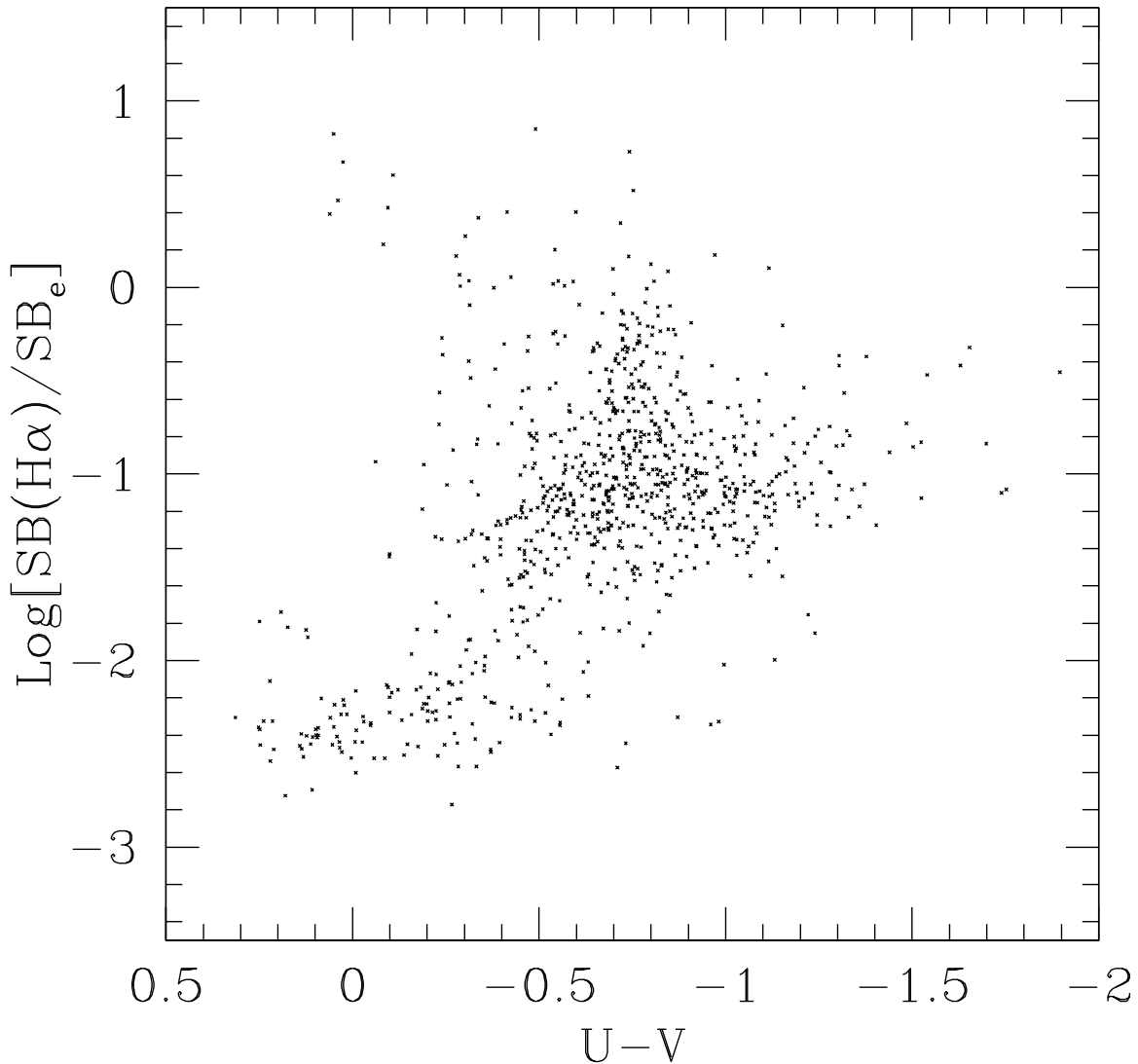


Fig. 9.— The H α surface brightness (normalized to the mean half-light radius surface brightness) as a function of the U–V color of the starburst population, for the same bins of Figure 3. The U and V band emission of the underlying $r^{1/4}$ stellar population has been removed. As expected, there is a trend for regions of higher H α surface brightness to have bluer U–V color. Regions with $\text{SB}(\text{H}\alpha)/\text{SB}_e < 0.01$ correspond to nonionizing or only weakly ionizing stellar populations. The region occupied by the starburst population is only a fraction of the area of the ionized gas emission.

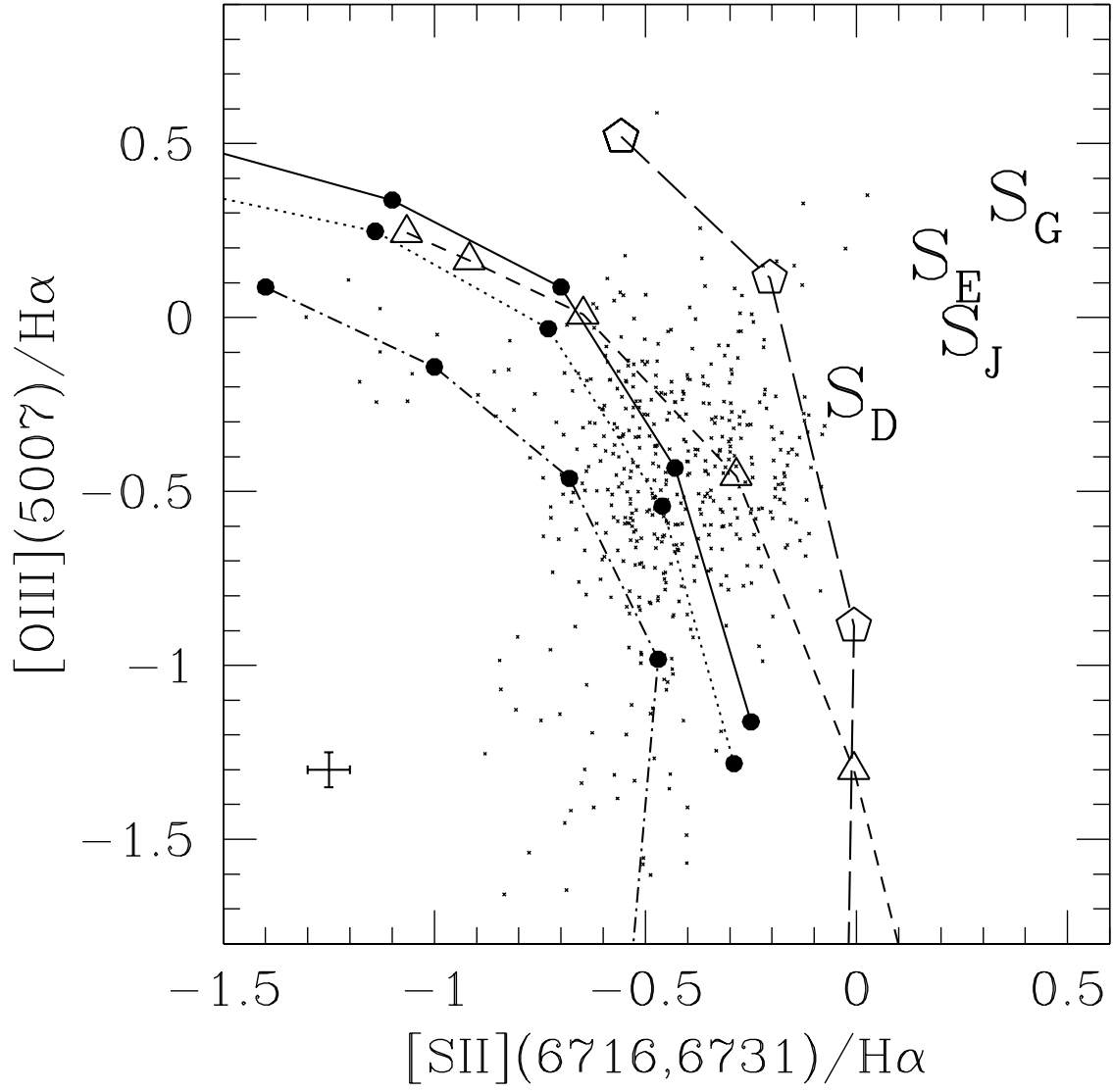


Fig. 10.— As Figure 5 (panel a), for NGC5236. Note that the vertical axis reports $\log([OIII]/H\alpha)$ instead of $\log([OIII]/H\beta)$. Models are scaled accordingly.

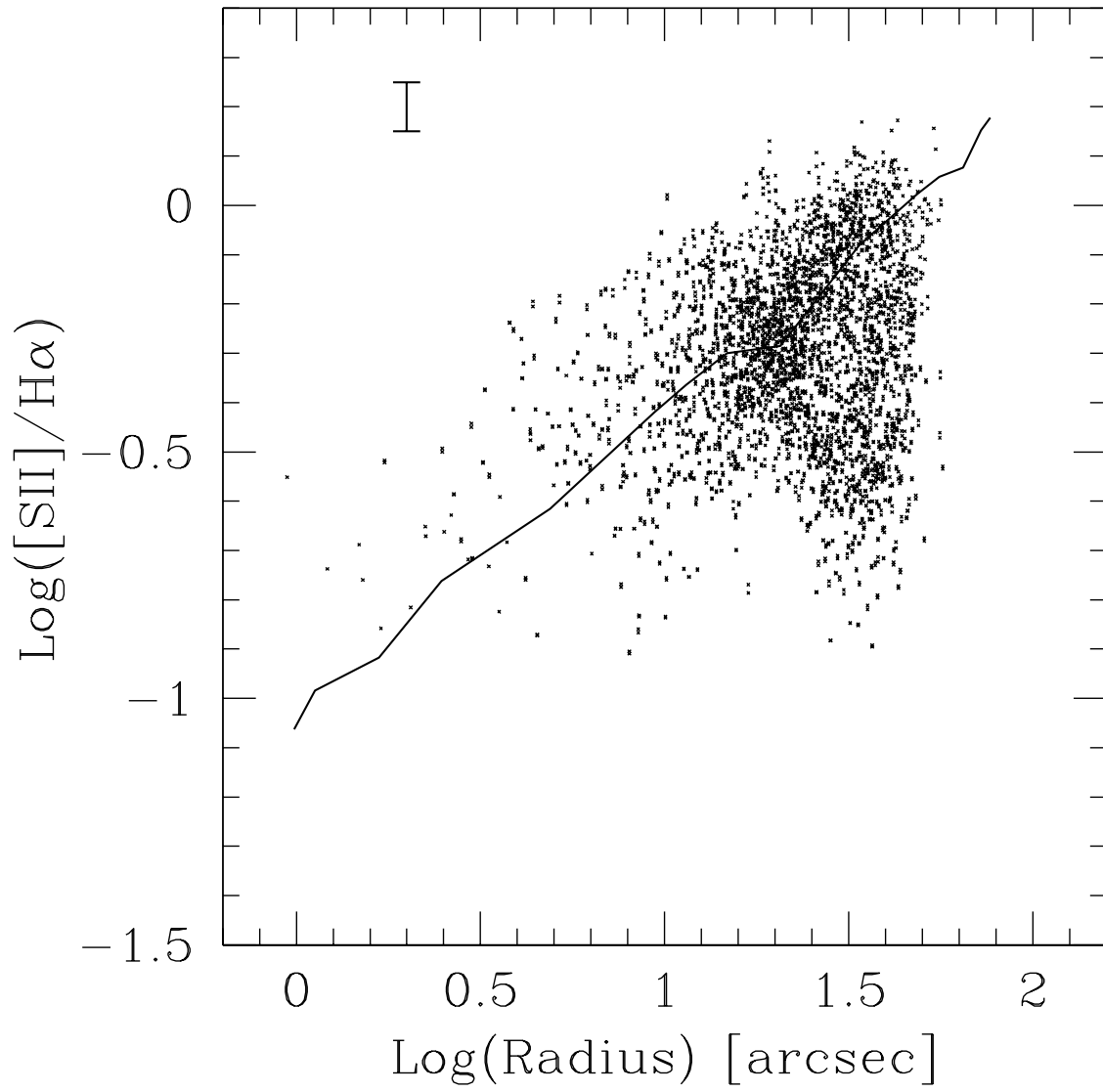


Fig. 11a.— (see next page for caption)

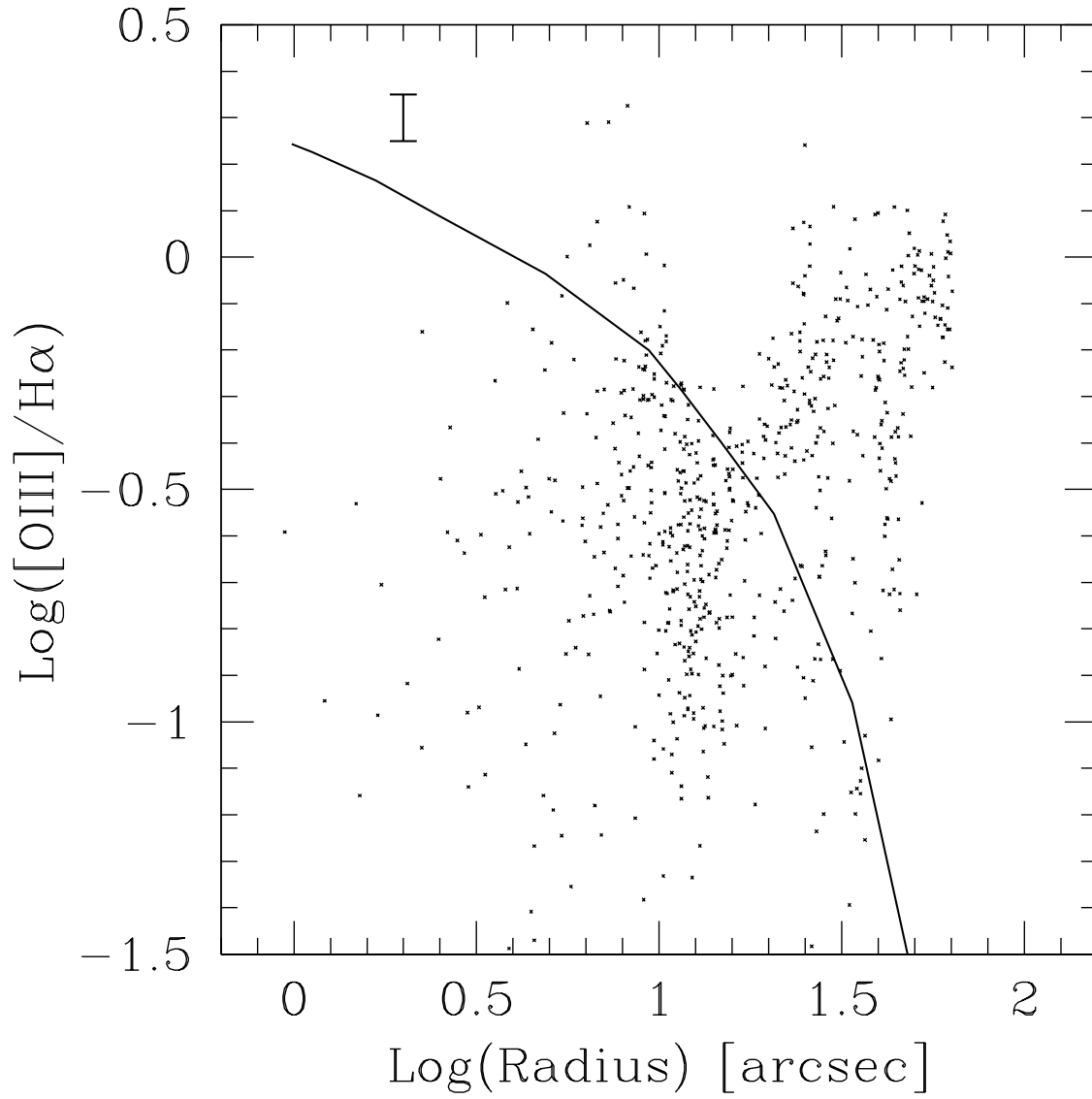


Fig. 11b.— As Figure 6, for NGC5236. Note that the vertical axis of Fig. 11b reports $\log([\text{OIII}]/\text{H}\alpha)$ instead of $\log([\text{OIII}]/\text{H}\beta)$. Models are scaled accordingly.

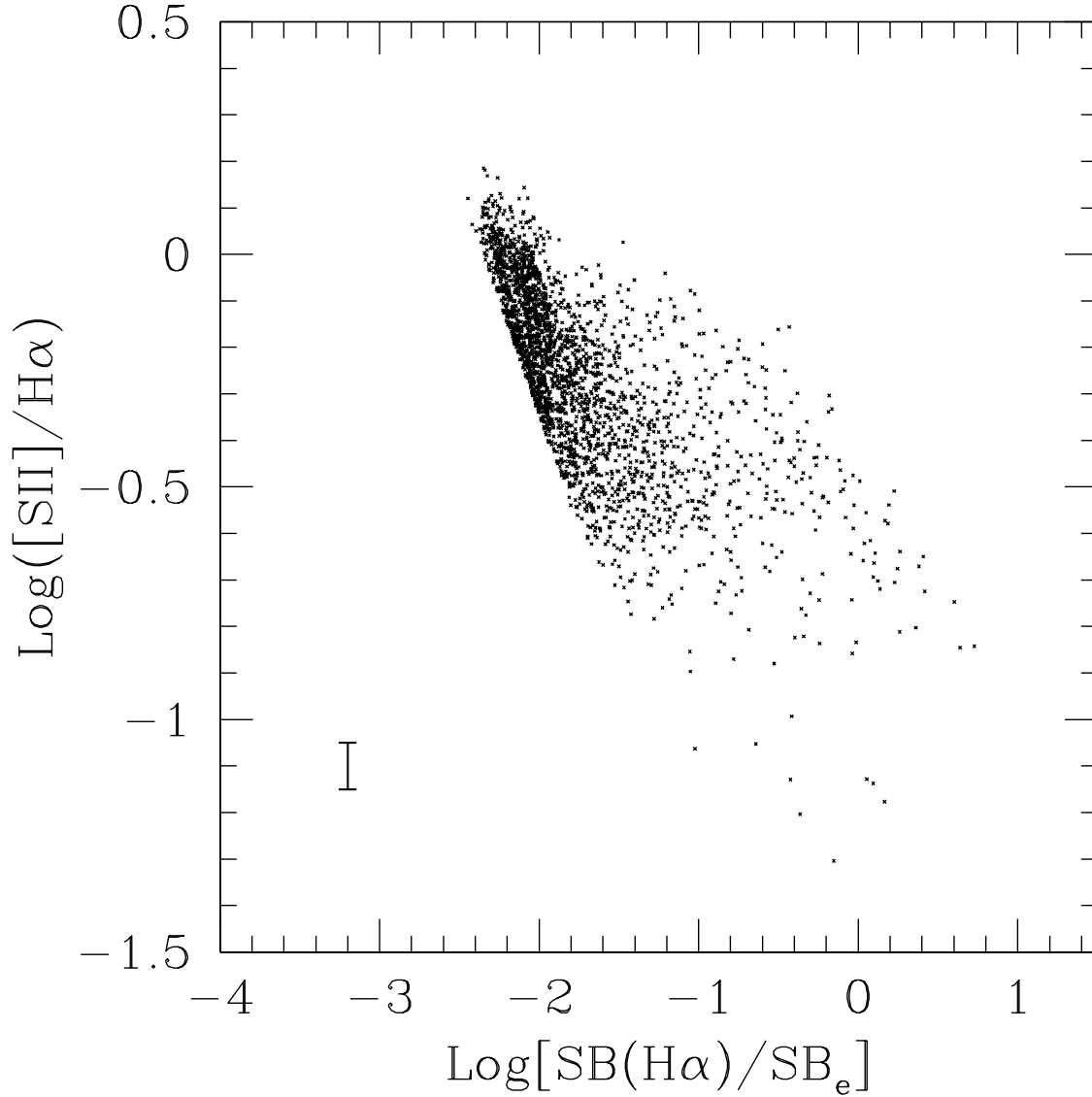


Fig. 12.— As Figure 7, for NGC5236. In this galaxy, the $\text{H}\alpha$ surface brightness within the half-light radius is $3.47 \text{ E-14 erg s}^{-1} \text{ cm}^{-2} \text{ arcsec}^{-2}$, which, after correction for a color excess $E(\text{B-V})=0.35$, becomes $\text{SB}_e=7.69 \text{ E-14 erg s}^{-1} \text{ cm}^{-2} \text{ arcsec}^{-2}$. The *observed* half-light radius $\text{H}\alpha$ surface brightness for this galaxy is a factor ~ 1.8 smaller than in NGC5253.

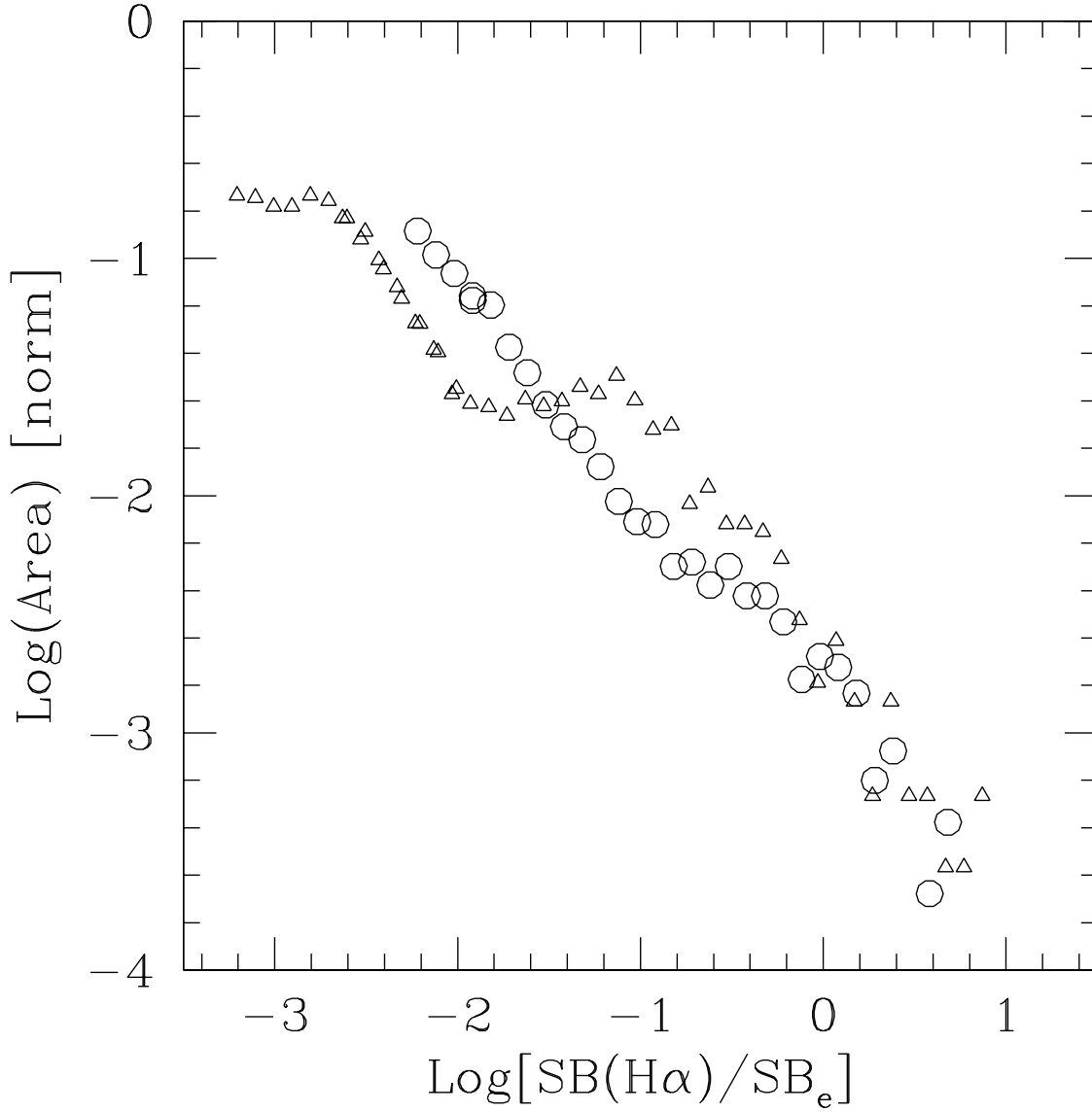


Fig. 13.— As Figure 8, for NGC5236 (circles). In this case, the data points are corrected for both underlying stellar absorption and dust reddening. For comparison, the data points for NGC5253 are also reported from Figure 8 (triangles). Unlike the case of NGC5253, no ‘natural’ break in the trend is visible here, except, possibly, for some hint at $\text{SB}(\text{H}\alpha)/\text{SB}_e \simeq 0.15$.

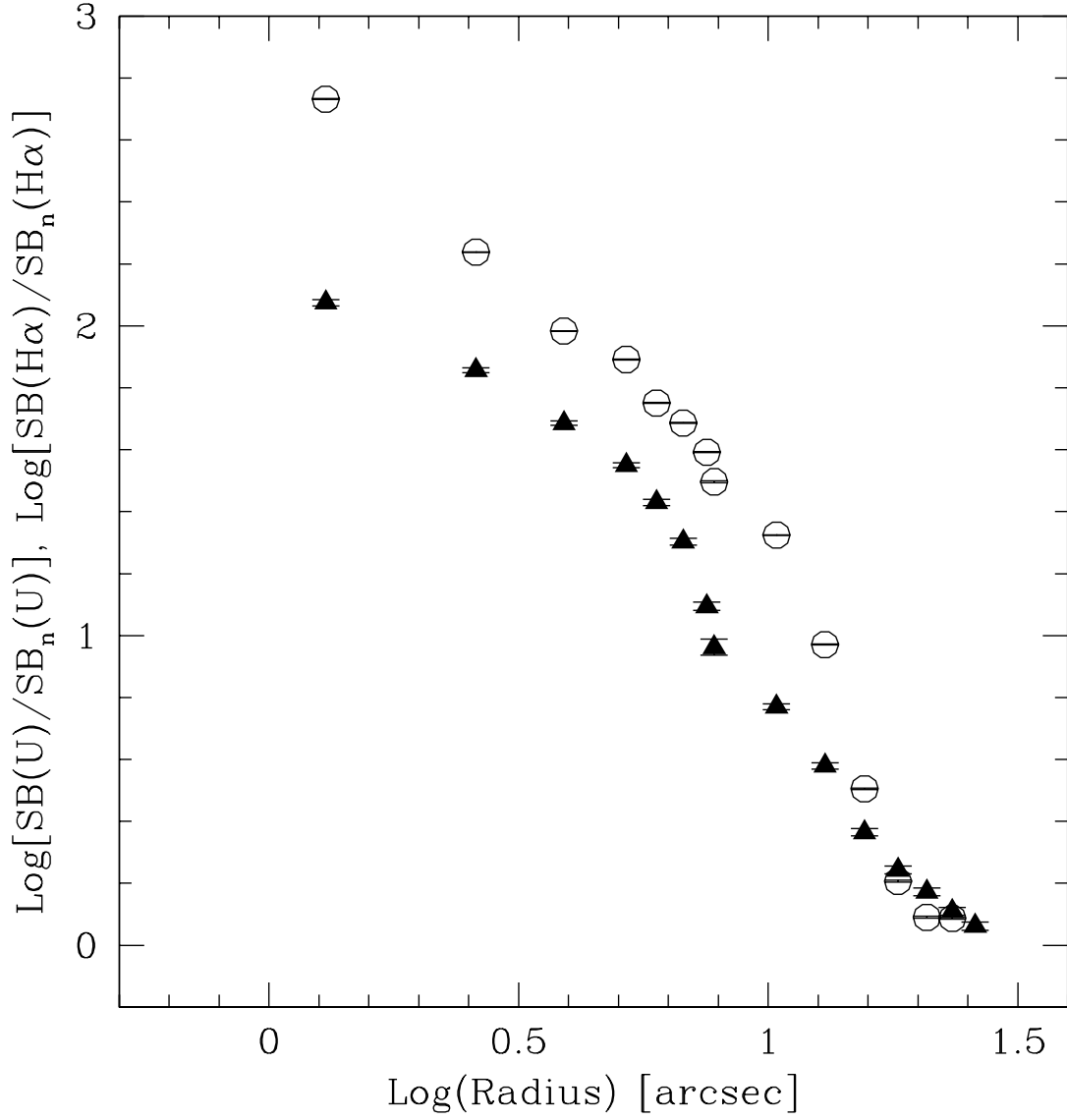


Fig. 14.— The azimuthally-averaged surface brightness profiles of both H α and U-band emission in annuli of increasing distance from peak of emission. Both profiles are normalized to the mean value of an annulus $\sim 7''$ wide at a distance $\sim 30''$ from the emission peak. The similarity of the two profiles is striking, despite the larger obscuring effects of dust in the U-band relative to the H α .

This figure "Calzetti.fig1.jpg" is available in "jpg" format from:

<http://arxiv.org/ps/astro-ph/9904428v1>

This figure "Calzetti.fig2a.jpg" is available in "jpg" format from:

<http://arxiv.org/ps/astro-ph/9904428v1>

This figure "Calzetti.fig2b.jpg" is available in "jpg" format from:

<http://arxiv.org/ps/astro-ph/9904428v1>

This figure "Calzetti.fig3a.jpg" is available in "jpg" format from:

<http://arxiv.org/ps/astro-ph/9904428v1>

This figure "Calzetti.fig3b.jpg" is available in "jpg" format from:

<http://arxiv.org/ps/astro-ph/9904428v1>

This figure "Calzetti.fig4.jpg" is available in "jpg" format from:

<http://arxiv.org/ps/astro-ph/9904428v1>